Droplet motion in one-component fluids on solid substrates with wettability gradients

Xinpeng Xu[1] and Tiezheng Qian[2,*]

[1]*Nano Science and Technology (NSNT) Program, Hong Kong University of Science and Technology, Clear Water Bay, Kowloon, Hong Kong*

[2]*Department of Mathematics and KAUST-HKUST Micro/Nanofluidics Joint Laboratory, Hong Kong University of Science and Technology, Clear Water Bay, Kowloon, Hong Kong*

(Received 3 January 2012; revised manuscript received 29 March 2012; published 11 May 2012)

Droplet motion on solid substrates has been widely studied not only because of its importance in fundamental research but also because of its promising potentials in droplet-based devices developed for various applications in chemistry, biology, and industry. In this paper, we investigate the motion of an evaporating droplet in one-component fluids on a solid substrate with a wettability gradient. As is well known, there are two major difficulties in the continuum description of fluid flows and heat fluxes near the contact line of droplets on solid substrates, namely, the hydrodynamic (stress) singularity and thermal singularity. To model the droplet motion, we use the dynamic van der Waals theory [Phys. Rev. E **75**, 036304 (2007)] for the hydrodynamic equations in the bulk region, supplemented with the boundary conditions at the fluid-solid interface. In this continuum hydrodynamic model, various physical processes involved in the droplet motion can be taken into account simultaneously, e.g., phase transitions (evaporation or condensation), capillary flows, fluid velocity slip, and substrate cooling or heating. Due to the use of the phase field method (diffuse interface method), the hydrodynamic and thermal singularities are resolved automatically. Furthermore, in the dynamic van der Waals theory, the evaporation or condensation rate at the liquid-gas interface is an outcome of the calculation rather than a prerequisite as in most of the other models proposed for evaporating droplets. Numerical results show that the droplet migrates in the direction of increasing wettability on the solid substrates. The migration velocity of the droplet is found to be proportional to the wettability gradients as predicted by Brochard [Langmuir **5**, 432 (1989)]. The proportionality coefficient is found to be linearly dependent on the ratio of slip length to initial droplet radius. These results indicate that the steady migration of the droplets results from the balance between the (conservative) driving force due to the wettability gradient and the (dissipative) viscous drag force. In addition, we study the motion of droplets on cooled or heated solid substrates with wettability gradients. The fast temperature variations from the solid to the fluid can be accurately described in the present approach. It is observed that accompanying the droplet migration, the contact lines move through phase transition and boundary velocity slip with their relative contributions mostly determined by the slip length. The results presented in this paper may lead to a more complete understanding of the droplet motion driven by wettability gradients with a detailed picture of the fluid flows and phase transitions in the vicinity of the moving contact line.

DOI: 10.1103/PhysRevE.85.051601 PACS number(s): 68.08.Bc, 47.61.−k, 05.70.Ln, 83.50.Lh

I. INTRODUCTION

Droplet motion on solid substrates is ubiquitous in nature [1,2]. Since the pioneering papers by Thomson [3] and Marangoni [4], an important body of work has been devoted to the study of droplet motion driven by the Marangoni effect, which is induced by the gradient of interfacial tension of the liquid-liquid or liquid-gas interface. It is equally important to study the droplet motion on solid surfaces with wettability gradients [5]. Great efforts have been made to improve our understanding of droplet motion not only because of its importance in fundamental research, but also because of its promising potentials in droplet-based devices developed for various applications in chemistry, biology, and industry [6–10]. Technologically, droplet motion on solid substrates can be triggered by thermal [11,12], chemical [13], electric [10], magnetic [14], and photoirradiative [15] methods. In the present paper, we focus on the case where the droplet motion is induced by the chemical or wettability gradients at solid surfaces. A gradient in wettability leads to the droplet motion in the direction of increasing wettability, which lowers the free energy of the system.

The droplet motion driven by wettability gradients was predicted by Greenspan [5] and was investigated by Brochard [16] and Raphael [17]. Their predictions have been confirmed experimentally [13,15,18–20] by using surfaces with various types of wettability gradients. According to Brochard [16], the forces acting on the droplet include the driving force due to the wettability gradient and the viscous drag force. To balance these two forces (with a negligible inertia effect), the droplet attains a steady state with an almost constant migration velocity V_{mig} given by [16,21,22]

$$V_{\mathrm{mig}} = \alpha_V \frac{\gamma h_0}{\eta} \frac{d \cos\ \theta_s}{dx}. \tag{1.1}$$

Here, γ and η are the surface tension and viscosity of the liquid, respectively, h_0 is the height of the droplet, θ_s is the static contact angle varying along the solid substrate, and the proportionality coefficient α_V is positive as droplets migrate from the low wettability region to the high wettability region spontaneously. The magnitude of α_V depends on the hydrodynamic mechanism that resolves the stress singularity at the three-phase contact line [5,16,22]. Theoretically, α_V is

*maqian@ust.hk.

a constant provided that the drag forces in the vicinity of the contact line scale with the fluid viscosity in the bulk region [22]. The relation (1.1) has been confirmed experimentally [22]. Note that the hydrodynamic mechanism is not directly implied by Eq. (1.1). The present paper shows that the droplet motion is driven by the gradient of Laplace pressure induced by the contact angle difference across the droplet.

It is worth pointing out that, in nearly all the previous theoretical papers, the droplet migration velocity and the forces acting on the droplet are derived using either the lubrication approximation or the wedge approximation. The lubrication approximation is usually used for nearly flat droplets and films [16,21], whereas, the wedge approximation treats the shape of a droplet as a collection of wedges [23]. Roughly speaking, the former involves a local balance of forces, whereas, the latter involves a balance of forces on the entire droplet [23]. A small θ_s, typically $\theta_s < 30^\circ$, is assumed in these approximations. However, in many practical situations, a substrate with varying wettability can produce contact angles that range from 100° down to 20° [24]. The other issue pertaining to evaporating droplets is the phase transition, which may play an essential role in controlling the droplet motion on solid substrates. Typically, an empirical relation is assumed and is used for the evaporation or condensation rate at the droplet surface in literature [25–27]. The above two issues concern the theoretical and numerical studies of evaporating droplets. As a matter of fact, the motion of evaporating droplets on solid substrates plays an important role in many industrial and medical applications, e.g., coating and printing technology [28]. Therefore, the study of evaporating droplets is highly nontrivial in both fundamental research and practical applications.

The motion of evaporative droplets on solid substrates naturally involves the fluid flows and heat fluxes near the contact line, the intersection of the droplet surface with the solid surface. It has been known for decades that the moving contact line presents challenges in its continuum description, namely, the hydrodynamic singularity and the thermal singularity [29–34]. The hydrodynamic singularity states that the fluid stress is nonintegrable at the moving contact line if the classical no-slip boundary condition is applied at the solid surface [29,30]. Two mechanisms have been proposed to resolve this stress singularity. The first is to introduce a velocity slip in a small region near the contact line [24,35–40], whereas, the second is to take into account the diffusive transport across the fluid-fluid interface in binary fluids [38,39,41,42] or the mass transport across the liquid-gas interface in one-component fluids [40,43]. In addition, the stress singularity can be removed if the (nominal) contact line is preceded by a thin precursor film [44]. The thermal singularity refers to the nonintegrable heat flux near the contact line in liquid-gas systems on heated or cooled solid substrates [31–34]. The heat flux tends to diverge at the contact line as the temperature exhibits a nearly discontinuous variation there. This is because the liquid-gas interface is almost isothermal at the coexistence or saturation temperature, while the solid surface is nearly isothermal for a highly conductive solid. Therefore, a temperature discontinuity is inevitable if the liquid-gas interface and the solid surface are of different temperatures and intersect at the contact line [43,45]. There exist three mechanisms that can be used to resolve this thermal singularity. (i) The temperature is allowed to vary along the liquid-gas interface [31]. (ii) The finite heat conductivity of the solid substrate is taken into consideration [31,46]. (iii) A temperature slip is introduced at the fluid-solid interface. Based on the above understanding, we believe that a continuum hydrodynamic model capable of resolving both the stress and the temperature singularities is imperative.

In this paper, we present a continuum hydrodynamic model suitable for the study of evaporating droplets in one-component fluids on solid substrates. We then carry out numerical simulations for evaporating droplets moving on solid substrates with wettability gradients. In constructing the model, we use the dynamic van der Waals theory developed by Onuki for one-component liquid-gas systems [43,45], supplemented with the hydrodynamic boundary conditions, which are derived based on the mechanical and thermodynamic principles [40,47].

The phase field model by Onuki [43,45] is closely related to the so-called model H, which was originally devised to describe the critical dynamics of thermal fluctuations [48,49]. For binary fluids, several variants of model H have been proposed to study thermocapillary flows [50], two-phase flows with a density contrast [51], and influence of convection on phase segregation [52]. The translation between several interrelated models was also discussed [53]. For one-component fluids, phase field models have been developed in Refs. [43,49] where the connections with model H have been addressed. The purpose of the present paper is to study the droplet motion in one-component fluids with liquid-gas transition in the nonisothermal situation. Therefore, we employ the model proposed by Onuki in which momentum transport, heat transport, and phase transition are coupled. Recently, this model has been used to study the thermohydrodynamics of boiling in one-component fluids [54]. It is interesting to note that the model by Anderson *et al.* [49] and that by Onuki [43] yield practically indistinguishable results for a boiling simulation in a domain with a temperature gradient [54].

It is worth emphasizing that the boundary conditions derived in the present paper represent a generalization of those in our previous paper [40] as the fluid-solid interface is no longer assumed to be isothermal here. In this continuum model, various physical processes involved in the droplet motion can be taken into account, including phase transitions (evaporation or condensation) and capillary flows in the bulk liquid-gas region [43,45], fluid velocity slip [24,35–40], temperature slip (namely, the Kapitza resistance) [55,56], and mechanical-thermal cross coupling [57] at the fluid-solid interface. It is also capable of describing the droplet motion for arbitrary contact angles. Furthermore, the hydrodynamic and thermal singularities can be resolved by the phase field (diffuse interface) description and the various interfacial processes inherent in the model. It is also worth pointing out that the evaporation or condensation rate at the liquid-gas interface is now a result of hydrodynamic calculations, rather than an empirical input as in most of the literature on evaporating droplets [58–62]. Therefore, this model has the potential of leading to a better understanding of evaporating droplets on solid substrates. From the numerical simulations for evaporating droplets on solid substrates with wettability

gradients, we measure the droplet migration velocity and analyze its dependence on wettability gradient, contact angle, boundary slip, and substrate temperature. We also observe that accompanying the droplet migration, the contact lines move through phase transition and boundary slip with their relative contributions tunable by slip length. This observation, now made at nonisothermal fluid-solid interfaces, is consistent with our previous observation for contact line motion at isothermal fluid-solid interfaces [40].

We would like to point out that, as a phase field model for one-component fluids, the dynamic van der Waals theory leads to a small interfacial thickness (∼1nm) at temperatures far away from the critical point. In this regime, the dynamic van der Waals theory is expected to approach the free-boundary formulation [58,63,64]. This may be demonstrated by taking the sharp interface limit [49–51,65,66]. For immiscible two-component (binary) fluids, this limit has been well studied, and comparisons have been made with free-boundary formulation [50,65,66]. For one-component fluids, an attempt of taking the sharp interface limit has been presented in Ref. [49], and more papers are to follow in this direction. In the present paper, we have only studied the motion of droplets on the nanoscale. We hope that our continuum results can motivate (i) molecular dynamics simulations for systems of comparable size and (ii) continuum simulations for much larger systems. Whether larger drops can be studied with an artificially thick liquid-gas interface remains an open question to be answered through a thorough study of the sharp interface limit of one-component fluid dynamics [49].

The paper is organized as follows. Following the introduction in Sec. I, Sec. II is devoted to a review of the dynamic van der Waals theory and a derivation of the necessary boundary conditions at the fluid-solid interface. In Sec. III, details of our numerical simulations are explained. In Sec. IV, the numerical results are presented and are discussed. The paper is concluded in Sec. V with a few remarks.

II. DYNAMIC VAN DER WAALS THEORY FOR ONE-COMPONENT FLUIDS ON SOLID SUBSTRATES

The first part of this section is a brief review of the dynamic van der Waals theory [43,67]. This theory assumes the local equilibrium condition for density at the solid boundary, the no-slip boundary condition for velocity, and the continuity conditions for temperature and heat flux normal to the fluid-solid interface. In the second part, these boundary conditions are relaxed by introducing additional dissipative processes at the fluid-solid interface [40,47]. The positive definiteness of entropy production rate is the guiding principle for formulating the hydrodynamic equations in the bulk region and the boundary conditions at the fluid-solid interface.

A. Hydrodynamic equations and constitutive relations

In a diffuse-interface modeling of one-component liquid-gas systems, the order parameter is the number density n, which takes distinct values in the liquid and gas phases and shows a fast variation across the liquid-gas interface. In order to describe the inhomogeneous systems, the contributions of density gradient are included in the entropy density $\hat{S}$ and the internal energy density $\hat{e}$ through

$$\hat{S} = ns(n,e) - \frac{C}{2}|\nabla n|^2, \tag{2.1}$$

$$\hat{e} = e + \frac{K}{2}|\nabla n|^2, \tag{2.2}$$

where $s(n,e)$ is the entropy per molecule in a homogeneous system of number density n and internal energy density e. Note that $\hat{S}$ and $\hat{e}$ both consist of a regular part for a homogeneous system [68] and a gradient part due to the inhomogeneity of the number density. Here, C and K are both positive, indicating a decrease in entropy and an increase in internal energy due to the density variations. In general, C and K may depend on n, i.e., $C = C(n)$ and $K = K(n)$. Note that the dynamic van der Waals theory has been presented to describe the hydrodynamics in one-component fluids with a liquid-gas transition in the nonisothermal situation. For this purpose, the gradient contribution to the internal energy and that to the entropy have to be introduced respectively. In the isothermal situation, the gradient contributions to energy and entropy can be combined in the Helmholtz free energy in describing the statics and dynamics, consistent with the general thermodynamic consideration. This leads to the coefficient $M = K + CT$ with $T =$ constant. (Note that this coefficient will appear in the equilibrium conditions derived below.) In the seminal paper of Cahn and Hilliard [69], the interfacial structures were studied for isothermal systems by introducing a Helmholtz free energy with a square gradient term. The coefficient κ in this gradient term corresponds to M in our approach. It is worth emphasizing that, in the isothermal situation, only κ (or M) is needed as a parameter, which, in general, may be dependent on local density and temperature. However, in the nonisothermal situation, K and C need to be introduced into the internal energy and the entropy, respectively. In our paper, $K = 0$ and $C =$ constant have been used for simplicity. These assumptions were also used by Onuki [43,45]. Recently, the dynamic van der Waals theory has been employed to study the thermohydrodynamics of boiling by assuming $C = 0$ and $K =$ constant [54].

In the van der Waals theory for homogeneous one-component fluids [68], the entropy per molecule s, the internal energy density e, and the pressure p can be expressed as functions of number density n and temperature T,

$$s(n,T) = k_B \ln[(k_BT/\varepsilon)^{3/2}(1/nv_0 - 1)] + s_0, \tag{2.3}$$

$$e(n,T) = 3nk_BT/2 - \varepsilon v_0 n^2, \tag{2.4}$$

$$p(n,T) = nk_BT/(1 - v_0 n) - \varepsilon v_0 n^2, \tag{2.5}$$

where k_B is the Boltzmann constant, ε is the strength of attractive interaction, v_0 is the molecular volume, and $s_0 = 5k_B/2 + k_B \ln[v_0(\varepsilon m/2\pi\hbar^2)^{3/2}]$ with m being the molecular mass. In this mean field theory for liquid-gas phase transition, the critical temperature and critical density are given by $T_c = 8\varepsilon/27k_B$, $n_c = 1/3v_0$, respectively. Equations (2.3)–(2.5) can be derived from the Helmholtz free energy density $f(n,T) = nk_BT[\ln(\lambda_{\rm th}^3 n) - 1 - \ln(1 - v_0 n)] - \varepsilon v_0 n^2$ by using the standard thermodynamic relations. Here, $\lambda_{\rm th} = \hbar(2\pi/mk_BT)^{1/2}$ is the thermal de Broglie wavelength. Physically, s_0 is a constant

independent of n and T (and, hence, does not show up in the balance equation for entropy), $e(n,T)$ consists of the kinetic energy due to random molecular motion and the attractive potential energy, and the expression for $p(n,T)$ is the equation of state exhibiting liquid-gas coexistence.

To derive the equilibrium conditions in the bulk region, we consider a system of entropy $S_b = \int d\mathbf{r}\, \hat{S}$ with fixed particle number $N = \int d\mathbf{r}\, n$ and fixed internal energy $E_b = \int d\mathbf{r}\, \hat{e}$. Maximizing S_b with respect to $\hat{e}$ and n yields the bulk equilibrium conditions: (i) the homogeneity of temperature T and (ii) the homogeneity of the generalized chemical potential,

$$\hat{\mu} = \mu + \frac{M_n}{2}|\nabla n|^2 - T\nabla\cdot\left(\frac{M}{T}\nabla n\right), \tag{2.6}$$

with $M(n,T) = K(n) + C(n)T$ and $M_n \equiv (\partial M/\partial n)_T$. Here, $\mu \equiv -T[\partial(ns)/\partial n]_e$ is the usual chemical potential for homogeneous fluids. We then introduce the generalized pressure $\hat{p}$ through the generalized Euler equation,

$$\hat{e} - T\hat{S} + \hat{p} - n\hat{\mu} = 0, \tag{2.7}$$

with

$$\hat{p} = p - \frac{M}{2}|\nabla n|^2 + \frac{nM_n}{2}|\nabla n|^2 - Tn\nabla n\cdot\nabla\frac{M}{T} - Mn\nabla^2 n. \tag{2.8}$$

Now, we turn to the hydrodynamic equations, which can be derived from the balance equations for particle number, momentum, and energy, supplemented with the constitutive relations for viscous stress and heat flux [43]. The mass density $\rho \equiv mn$, the momentum density $\rho\mathbf{v}$, and the total energy density $e_T \equiv \hat{e} + \rho\mathbf{v}^2/2$ obey the hydrodynamic equations,

$$\frac{\partial n}{\partial t} + \nabla\cdot(n\mathbf{v}) = 0, \tag{2.9}$$

$$\frac{\partial}{\partial t}(\rho\mathbf{v}) + \nabla\cdot(\rho\mathbf{v}\mathbf{v}) = \nabla\cdot\overleftrightarrow{\mathbf{M}}, \tag{2.10}$$

$$\frac{\partial e_T}{\partial t} + \nabla\cdot(e_T\mathbf{v}) = -\nabla\cdot\left(-\overleftrightarrow{\mathbf{M}}\cdot\mathbf{v} + \mathbf{q}\right), \tag{2.11}$$

respectively, with $\overleftrightarrow{\mathbf{M}} = -\overleftrightarrow{\Pi} + \overleftrightarrow{\sigma}$ being the total stress tensor. Here, the reversible stress tensor $-\overleftrightarrow{\Pi}$, the viscous stress tensor $\overleftrightarrow{\sigma}$, and the heat flux $\mathbf{q}$ are given by

$$-\overleftrightarrow{\Pi} = -M\nabla n\nabla n - \hat{p}\overleftrightarrow{\mathbf{I}}, \tag{2.12}$$

$$\overleftrightarrow{\sigma} = \eta(\nabla\mathbf{v} + \nabla\mathbf{v}^T) + (\zeta - 2\eta/3)\overleftrightarrow{\mathbf{I}}\nabla\cdot\mathbf{v}, \tag{2.13}$$

$$\mathbf{q} = -\lambda\nabla T, \tag{2.14}$$

respectively, with $\hat{p}$ expressed in Eq. (2.8). The positive coefficients η, ζ, and λ denote the shear viscosity, bulk viscosity, and heat conductivity, respectively. In order to update the temperature distribution, we solve the balance equation for entropy density $\hat{S}$,

$$\frac{\partial\hat{S}}{\partial t} + \nabla\cdot(\hat{S}\mathbf{v}) = -\nabla\cdot\hat{\mathbf{J}}_f^S + \frac{1}{T}\overleftrightarrow{\sigma} : \nabla\mathbf{v} - \frac{1}{T^2}\mathbf{q}\cdot\nabla T, \tag{2.15}$$

instead of the energy equation (2.11). This is to avoid the artificial parasitic flows in numerical computation [70]. Here, $\hat{\mathbf{J}}_f^S \equiv [\mathbf{q} + M(\partial n/\partial t + \mathbf{v}\cdot\nabla n)\nabla n]/T$ represents the total (reversible) entropy flux, which includes the contribution of the inhomogeneity of number density, given by $M(\partial n/\partial t + \mathbf{v}\cdot\nabla n)\nabla n$. The local relation between T and $\hat{S}$ is

$$\left(\frac{k_BT}{\varepsilon}\right)^{3/2} = \frac{nv_0}{1-nv_0}\exp\left(\frac{\hat{S} + C|\nabla n|^2/2}{nk_B}\right), \tag{2.16}$$

which is obtained from Eqs. (2.1) and (2.3). Here, the constant s_0 in Eq. (2.3) is omitted because $\hat{S}$ is determined up to $n\times$ constant by Eq. (2.15) due to the continuity equation (2.9).

In the hydrodynamic description outlined above, the liquid-gas phase transition is represented by the converging (for condensation) or diverging (for evaporation) velocity field, the liquid-gas interfacial tension is realized through the anisotropic part $-M\nabla n\nabla n$ in the reversible stress tensor $-\overleftrightarrow{\Pi}$, and the latent heat release or absorption is described by the balance equation for entropy. That is, the entropy change arising from phase transition is accompanied by the heat flux $\mathbf{q}$ that enters into the entropy flux $\hat{\mathbf{J}}_f^S$.

B. Hydrodynamic boundary conditions

The hydrodynamic boundary conditions derived here represent a generalization of those in our previous paper [40] where the fluid-solid interface is assumed to be isothermal. The equilibrium and dynamic properties of a fluid can be considerably modified by its interactions with the solid substrate. Following our previous paper [40], the solid substrate is modeled to be flat, rigid, impermeable, and insoluble. The temperature in the solid substrate, hereafter denoted by T_w, obeys the heat equation,

$$C_w\frac{\partial T_w}{\partial t} = \lambda_w\nabla^2 T_w, \tag{2.17}$$

where C_w is the heat capacity (per unit volume) and λ_w is the heat conductivity of the solid with $\mathbf{q}_w = -\lambda_w\nabla T_w$ being the heat flux in the solid. Note that Eq. (2.17) is valid only in the reference frame moving with the rigid solid substrate. In general, $\partial T_w/\partial t$ should be replaced by $dT_w/dt = \partial T_w/\partial t + \mathbf{w}\cdot\nabla T_w$ with $\mathbf{w}$ denoting the velocity of the substrate. For simplicity, here, we choose the reference frame moving with the solid substrate, and hence, $\mathbf{w} = 0$. Moreover, for the purpose of the present paper, we only consider the situation where T_w is fixed and homogeneous (in the limit of $\lambda_w \to \infty$). Since the solid substrate is flat, rigid, and impermeable, we have the kinematic boundary condition for the normal components of the fluid velocity $\mathbf{v}$ and wall velocity $\mathbf{w}$ at the fluid-solid interface,

$$v_\gamma = w_\gamma, \tag{2.18}$$

with $v_\gamma \equiv \hat{\boldsymbol{\gamma}}\cdot\mathbf{v}$ and $w_\gamma \equiv \hat{\boldsymbol{\gamma}}\cdot\mathbf{w}$. However, the tangential components of these two boundary velocities may differ. That is, slip may occur at the fluid-solid interface, and the (tangential) slip velocity is defined as

$$\mathbf{v}_\tau^{\rm slip} = \mathbf{v}_\tau - \mathbf{w}_\tau, \tag{2.19}$$

with $\mathbf{v}_\tau = \mathbf{v} - v_\gamma\hat{\boldsymbol{\gamma}}$ and $\mathbf{w}_\tau = \mathbf{w} - w_\gamma\hat{\boldsymbol{\gamma}}$. In the reference frame moving with the solid substrate, the conditions (2.18) and (2.19) give $v_\gamma = 0$ and $\mathbf{v}_\tau^{\rm slip} = \mathbf{v}_\tau$.

For one-component liquid-gas flows on solid substrates, the boundary effects can be taken into account by introducing the surface entropy S_s and surface energy E_s as

$$S_s = \int dA\, \sigma_s'(n), \tag{2.20}$$

$$E_s = \int dA\, e_s'(n), \tag{2.21}$$

where σ_s' and e_s' are the surface entropy and surface energy per unit area and $\int dA$ denotes the surface integral at the fluid-solid interface [43]. Note that σ_s' and e_s' are only functions of n, the boundary value of fluid density. Here, the primes are used to denote the surface quantities whose dimensions are different from the corresponding bulk quantities. The Helmholtz free energy per unit area is given by

$$f_s'(n,T) = e_s'(n) - T\sigma_s'(n), \tag{2.22}$$

with T being the boundary value of fluid temperature at the fluid-solid interface. It follows that $\sigma_s' = -(\partial f_s'/\partial T)_n$, and hence,

$$df_s' = -\sigma_s' dT + \left(\frac{\partial f_s'}{\partial n}\right)_T dn. \tag{2.23}$$

Substituting Eq. (2.22) into Eq. (2.23) then gives a Gibbs-type equation,

$$d\sigma_s' = \frac{1}{T} de_s' - \frac{1}{T}\left(\frac{\partial f_s'}{\partial n}\right)_T dn. \tag{2.24}$$

Furthermore, the fluid-solid interfacial tension, denoted by γ_{fs}, satisfies a Euler-type equation $e_s' - T\sigma_s' - \gamma_{fs} = 0$ [71]. It follows that

$$\gamma_{fs} = f_s', \tag{2.25}$$

which depends on the local temperature.

To derive the equilibrium condition at the fluid-solid interface, we make use of the equilibrium conditions in the bulk region and minimize the total free energy $(E_b - TS_b) + (E_s - TS_s)$. This leads to

$$L \equiv M\nabla_\gamma n + \left(\frac{\partial f_s'}{\partial n}\right)_T = 0, \tag{2.26}$$

at the fluid-solid interface. Here, the scalar operator ∇_γ is defined by $\nabla_\gamma \equiv \hat{\boldsymbol{\gamma}} \cdot \nabla$ with $\hat{\boldsymbol{\gamma}}$ denoting the outward unit vector normal to the interface.

The hydrodynamic boundary conditions at the fluid-solid interface can be derived from the balance equations for particle number, momentum, and energy, supplemented with the positive definiteness condition for the rate of entropy production [40,47]. Here, it is assumed that the surface stress tensor $\overleftrightarrow{\mathbf{M}}'_s$ and surface heat flux $\mathbf{q}'_s$ (tangent to the surface) exist at the fluid-solid interface. But there is no surface viscosity. That is, $\overleftrightarrow{\mathbf{M}}'_s$ only has the reversible part arising from the interfacial tension γ_{fs},

$$\overleftrightarrow{\mathbf{M}}'_s \equiv \gamma_{fs}\overleftrightarrow{\tau} = f_s'\overleftrightarrow{\tau}, \tag{2.27}$$

with $\overleftrightarrow{\boldsymbol{\tau}} \equiv \overleftrightarrow{\mathbf{I}} - \hat{\boldsymbol{\gamma}}\hat{\boldsymbol{\gamma}}$ and $\overleftrightarrow{\mathbf{I}}$ being the identity tensor. Then, the equation for local force balance at the interface is given by

$$\nabla_\tau f_s' - \hat{\boldsymbol{\gamma}} \cdot \overleftrightarrow{\mathbf{M}} + \mathbf{F} = 0, \tag{2.28}$$

whose tangential and normal components are

$$\nabla_\tau f_s' - \hat{\boldsymbol{\gamma}} \cdot \overleftrightarrow{\mathbf{M}} \cdot \overleftrightarrow{\boldsymbol{\tau}} + \mathbf{F}_\tau = 0, \tag{2.29}$$

and

$$-\hat{\boldsymbol{\gamma}} \cdot \overleftrightarrow{\mathbf{M}} \cdot \hat{\boldsymbol{\gamma}} + F_\gamma = 0, \tag{2.30}$$

respectively, with $\overleftrightarrow{\mathbf{M}} = -\overleftrightarrow{\boldsymbol{\Pi}} + \overleftrightarrow{\boldsymbol{\sigma}}$ being the total stress tensor in the bulk fluid region. Here, $\nabla_\tau f_s' \equiv \nabla_\tau \cdot (f_s'\overleftrightarrow{\boldsymbol{\tau}})$ with the surface divergence of a vector field $\mathbf{a}$ defined by $\nabla_\tau \cdot \mathbf{a} \equiv \nabla \cdot \mathbf{a} - \nabla_\gamma(\hat{\boldsymbol{\gamma}} \cdot \mathbf{a})$, and $\mathbf{F}$ is the stress force exerted by the solid with $F_\gamma \equiv \hat{\boldsymbol{\gamma}} \cdot \mathbf{F}$ and $\mathbf{F}_\tau = \overleftrightarrow{\boldsymbol{\tau}} \cdot \mathbf{F}$ being the normal (scalar) and tangential (vector) wall forces (per unit area), respectively.

In the reference frame moving with the solid substrate, the equation for the local energy balance at the interface is given by

$$\frac{\partial e_s'}{\partial t} + \nabla_\tau \cdot (e_s'\mathbf{v}_\tau) = \nabla_\tau \cdot (\overleftrightarrow{\mathbf{M}}'_s \cdot \mathbf{v}_\tau) - \nabla_\tau \cdot \mathbf{q}'_s + (\hat{\boldsymbol{\gamma}} \cdot \mathbf{q} - \hat{\boldsymbol{\gamma}} \cdot \mathbf{q}_w) - \hat{\boldsymbol{\gamma}} \cdot \overleftrightarrow{\mathbf{M}} \cdot \mathbf{v}, \tag{2.31}$$

where the surface heat flux $\mathbf{q}'_s$ is actually defined through the nonconvective surface energy flux $-\overleftrightarrow{\mathbf{M}}'_s \cdot \mathbf{v} + \mathbf{q}'_s$. Substituting Eqs. (2.27) and (2.28) into Eq. (2.31), we obtain

$$\frac{\partial e_s'}{\partial t} + \nabla_\tau \cdot (e_s'\mathbf{v}_\tau) = \nabla_\tau \cdot (f_s'\mathbf{v}_\tau) - \nabla_\tau \cdot \mathbf{q}'_s + (\hat{\boldsymbol{\gamma}} \cdot \mathbf{q} - \hat{\boldsymbol{\gamma}} \cdot \mathbf{q}_w) - \hat{\boldsymbol{\gamma}} \cdot \overleftrightarrow{\mathbf{M}} \cdot \mathbf{v}_\tau^{\text{slip}}, \tag{2.32}$$

with $\mathbf{v}_\tau^{\text{slip}} = \mathbf{v}_\tau$ as defined in Eq. (2.19).

Using the Gibbs-type equation (2.24) for $\partial\sigma_s'/\partial t$, we can obtain the balance equation for the surface entropy density σ_s',

$$\frac{\partial \sigma_s'}{\partial t} + \nabla_\tau \cdot (\sigma_s'\mathbf{v}_\tau) = -\nabla_\tau \cdot \left(\frac{\mathbf{q}'_s}{T}\right) + \left(\hat{\boldsymbol{\gamma}} \cdot \hat{\mathbf{J}}_f^S - \frac{1}{T_w}\hat{\boldsymbol{\gamma}} \cdot \mathbf{q}_w\right) + \mathbf{q}'_s \cdot \nabla_\tau \frac{1}{T} - \left(\frac{1}{T} - \frac{1}{T_w}\right)\hat{\boldsymbol{\gamma}} \cdot \mathbf{q}_w - \frac{1}{T}\mathbf{F}_\tau \cdot \mathbf{v}_\tau^{\text{slip}} - \frac{1}{T}L\dot{n}, \tag{2.33}$$

where $\hat{\boldsymbol{\gamma}} \cdot \hat{\mathbf{J}}_f^S \equiv (\hat{\boldsymbol{\gamma}} \cdot \mathbf{q} + M\dot{n}\nabla_\gamma n)/T$ is the total entropy flux from the bulk fluid region, $\dot{n} \equiv \partial n/\partial t + \mathbf{v}_\tau \cdot \nabla_\tau n$ is the material derivative of n at the fluid-solid interface, and $L = M\nabla_\gamma n + (\partial f_s'/\partial n)_T$ is the quantity first defined in Eq. (2.26). It follows that the rate of entropy production per unit area at the fluid-solid interface is of the form

$$\sigma_{\text{surf}} \equiv \mathbf{q}'_s \cdot \nabla_\tau \frac{1}{T} - \left(\frac{1}{T} - \frac{1}{T_w}\right)\hat{\boldsymbol{\gamma}} \cdot \mathbf{q}_w - \frac{1}{T}\mathbf{F}_\tau \cdot \mathbf{v}_\tau^{\text{slip}} - \frac{1}{T}L\dot{n}, \tag{2.34}$$

which must be positive definite according to the second law of thermodynamics.

The surface entropy production σ_{surf} has already been written in the bilinear form in terms of the conjugate forces and fluxes. Among the four force-flux pairs, $\mathbf{q}'_s \cdot \nabla_\tau(1/T)$ and $-\mathbf{F}_\tau \cdot \mathbf{v}_\tau/T$ involve tangential vectors, whereas,

$-(1/T-1/T_w)\hat{\boldsymbol{\gamma}}\cdot\mathbf{q}_w$ and $-L\dot{n}/T$ involve scalars. In the linear response regime [72,73], the constitutive relations governing the interfacial dissipative processes can be obtained from Eq. (2.34). According to Curie's symmetry principle [73], there can be cross coupling between the vectorial pairs $\mathbf{q}'_s\cdot\boldsymbol{\nabla}_\tau(1/T)$ and $-\mathbf{F}_\tau\cdot\mathbf{v}_\tau/T$ and/or between the scalarial pairs $-(1/T-1/T_w)\hat{\boldsymbol{\gamma}}\cdot\mathbf{q}_w$ and $-L\dot{n}/T$. Without cross coupling between the scalarial pairs, two constitutive relations can be obtained as

$$\kappa\hat{\boldsymbol{\gamma}}\cdot\mathbf{q}_w=-\left(\frac{1}{T}-\frac{1}{T_w}\right), \tag{2.35}$$

$$\alpha\dot{n}=-L, \tag{2.36}$$

where κ is an interfacial parameter directly related to the interfacial thermal resistance (namely, the Kapitza resistance) [55] and α is another interfacial parameter controlling the density relaxation at the solid surface [40]. The positive definiteness of $\sigma_{\rm surf}$ requires κ and α to be positive.

As to the two vectorial pairs, the constitutive relations, which take into account the cross coupling, can be written as

$$\mathbf{q}'_s=-\lambda'_s\boldsymbol{\nabla}_\tau T-\chi\mathbf{F}_\tau, \tag{2.37}$$

$$\beta\mathbf{v}_\tau^{\rm slip}=-\beta\frac{\chi}{T}\boldsymbol{\nabla}_\tau T-\mathbf{F}_\tau, \tag{2.38}$$

where λ'_s is the surface heat conductivity, β is the slip coefficient, and χ is a coefficient measuring the mechanical-thermal cross coupling. The positive definiteness of $\sigma_{\rm surf}$ requires λ'_s and β to be positive. However, the sign of χ cannot be simply determined by thermodynamic constraints. It is also interesting to note that, in the presence of mechanical-thermal coupling with $\chi\neq 0$, then, still required by the positive definiteness of entropy production, λ'_s must be nonzero for surface heat transport and β cannot reach $+\infty$, i.e., there has to be a certain amount of velocity slip. We expect that molecular dynamics simulations can reveal how χ is influenced by fluid-solid interactions at microscopic length scales [57,74,75].

Based on the interfacial constitutive relations derived above, we can present the hydrodynamic boundary conditions in the form that can be directly coupled with the hydrodynamic equations in the bulk region. Substituting the definition of L in Eq. (2.26) into Eq. (2.36), we obtain

$$\alpha\dot{n}=-M\boldsymbol{\nabla}_\gamma n-\left(\frac{\partial f'_s}{\partial n}\right)_T, \tag{2.39}$$

as the boundary condition for density relaxation at solid surfaces of the same form as that derived in our previous paper [40]. Substituting Eqs. (2.12), (2.13), (2.23), and (2.29) into Eq. (2.38), we obtain

$$\begin{aligned}\beta\mathbf{v}_\tau^{\rm slip}=&-\eta\boldsymbol{\nabla}_\gamma\mathbf{v}_\tau+\left[M\boldsymbol{\nabla}_\gamma n+\left(\frac{\partial f'_s}{\partial n}\right)_T\right]\\&\times\boldsymbol{\nabla}_\tau n-\left(\sigma'_s+\beta\frac{\chi}{T}\right)\boldsymbol{\nabla}_\tau T,\end{aligned} \tag{2.40}$$

as the slip boundary condition. This is a generalization of that derived in our previous paper where the fluid-solid interface was assumed to be isothermal [40]. Substituting $\mathbf{q}_w=-\lambda_w\boldsymbol{\nabla}T_w$ into Eq. (2.35), we obtain

$$\kappa\lambda_w\boldsymbol{\nabla}_\gamma T_w=\frac{1}{T}-\frac{1}{T_w}, \tag{2.41}$$

as the boundary condition for temperature slip across the fluid-solid interface. It serves as a boundary condition for the solid temperature T_w governed by Eq. (2.17). Substituting Eqs. (2.22), (2.14), $\mathbf{q}_w=-\lambda_w\boldsymbol{\nabla}T_w$, Eqs. (2.37), (2.29), and (2.38) into the energy equation (2.32), we obtain

$$\begin{aligned}-\lambda\boldsymbol{\nabla}_\gamma T+\lambda_w\boldsymbol{\nabla}_\gamma T_w=&\frac{\partial e'_s}{\partial t}+\boldsymbol{\nabla}_\tau\cdot(T\sigma'_s\mathbf{v}_\tau)+\mathbf{v}_\tau\cdot\boldsymbol{\nabla}_\tau f'_s\\&-\boldsymbol{\nabla}_\tau\cdot(\lambda'_s\boldsymbol{\nabla}_\tau T)-\frac{1}{\beta}\mathbf{F}_\tau\cdot\mathbf{F}_\tau\\&-\boldsymbol{\nabla}_\tau\cdot(\chi\mathbf{F}_\tau)-\frac{\chi}{T}\mathbf{F}_\tau\cdot\boldsymbol{\nabla}_\tau T,\end{aligned} \tag{2.42}$$

as the boundary condition for energy balance. Here, the tangential wall force $\mathbf{F}_\tau$ is given by $\mathbf{F}_\tau=\eta\boldsymbol{\nabla}_\gamma\mathbf{v}_\tau-M\boldsymbol{\nabla}_\gamma n\boldsymbol{\nabla}_\tau n-\boldsymbol{\nabla}_\tau f'_s$ according to Eq. (2.29), and $\boldsymbol{\nabla}_\tau f'_s$ is given by $\boldsymbol{\nabla}_\tau f'_s=-\sigma'_s\boldsymbol{\nabla}_\tau T+(\partial f'_s/\partial n)_T\boldsymbol{\nabla}_\tau n$ according to Eq. (2.23). In our previous paper, the fluid temperature was assumed to be a uniform constant at the fluid-solid interface (a Dirichlet condition for the fluid temperature T) [40]. Now, this assumption is replaced by Eq. (2.42), which serves as a boundary condition for the fluid temperature. In the limit of $\lambda_w\to\infty$, the solid temperature becomes a constant. But there is still heat exchange between the fluid and the solid with $\lambda_w\to\infty$, $\boldsymbol{\nabla}_\gamma T_w\to 0$, and $\kappa\lambda_w\boldsymbol{\nabla}_\gamma T_w=1/T-1/T_w$ remaining finite. It follows that, in the limit of $\lambda_w\to\infty$, the boundary condition applicable to the fluid temperature becomes

$$\begin{aligned}&-\lambda\boldsymbol{\nabla}_\gamma T+\kappa^{-1}\left(\frac{1}{T}-\frac{1}{T_w}\right)\\&\quad=\frac{\partial e'_s}{\partial t}+\boldsymbol{\nabla}_\tau\cdot(T\sigma'_s\mathbf{v}_\tau)+\mathbf{v}_\tau\cdot\boldsymbol{\nabla}_\tau f'_s-\boldsymbol{\nabla}_\tau\cdot(\lambda'_s\boldsymbol{\nabla}_\tau T)\\&\qquad-\frac{1}{\beta}\mathbf{F}_\tau\cdot\mathbf{F}_\tau-\boldsymbol{\nabla}_\tau\cdot(\chi\mathbf{F}_\tau)-\frac{\chi}{T}\mathbf{F}_\tau\cdot\boldsymbol{\nabla}_\tau T,\end{aligned} \tag{2.43}$$

which is obtained by substituting Eq. (2.41) into Eq. (2.42). For comparison, we mention that, in our previous paper [40], the fluid-solid interface is assumed to be isothermal, and consequently, the boundary condition for fluid temperature is simply the Dirichlet condition $T=T_w$ with T_w being a known constant.

III. NUMERICAL SIMULATIONS

A. Phenomenological parameters

To make our numerical simulations simple and specific, a few assumptions are made for the phenomenological parameters in the model [40,43,67]:

(a) C is a positive constant while K vanishes, and hence, $M=CT$.

(b) Transport coefficients in the bulk region may strongly depend on the density n. The shear viscosity η, bulk viscosity ζ, and heat conductivity λ are locally proportional to n, i.e., $\eta=\zeta=\nu mn$ and $\lambda=k_B\nu n$, where $\nu=\eta/\rho$ is the kinematic viscosity independent of n.

(c) The surface energy density e'_s is a constant, and the surface entropy density is given by $\sigma'_s=-c_s(n-n_c)$ with c_s being a constant independent of n and T. Then, the surface free energy density f'_s in Eq. (2.22) is given by

$f_s' = c_s T(n - n_c) + \text{const}$, with

$$\nabla_\tau f_s' = -\sigma_s' \nabla_\tau T + \left(\frac{\partial f_s'}{\partial n}\right)_T \nabla_\tau n = c_s(n - n_c)\nabla_\tau T + c_s T \nabla_\tau n. \quad (3.1)$$

For the fluid density at the solid surface, a relaxational boundary condition has been used [see Eq. (2.39)]. The rate of density relaxation is controlled by the parameter α. If α approaches zero, then the fast equilibration leads to $L \equiv M\nabla_\gamma n + (\partial f_s'/\partial n)_T \to 0$, which indicates that the density distribution approaches local equilibrium at solid surface. In Refs. [66,76,77], the boundary condition $M\nabla_\gamma n + (\partial f_s'/\partial n)_T = 0$ was used to represent a local equilibrium at a solid surface. In particular, a special form was used for the fluid-solid interfacial free energy density f_s' such that $\partial f_s'/\partial n = 0$ for the *bulk* value of density. As a consequence, $\nabla_\gamma n = 0$ at the surface. It follows that there will be neither enrichment nor depletion near the solid surface. In the present paper, a linear dependence of f_s' on the local density n is assumed. For comparison, it is noted that f_s' is usually expanded to second order in $n - n_c$ [43]. These energy functions typically lead to density enrichment or depletion near the solid surface and have been widely used in the study of wettability effects and wetting transitions following the pioneering paper of Cahn [78]. We point out that, for the parameter value used in the present paper, there is no enrichment layer that takes the role of a precursor film [44]. It is interesting to note that f_s' took the same form in Ref. [67] where the parameter value was chosen to realize the complete wetting condition for a precursor film to grow.

(d) The relaxation coefficient α is a positive constant independent of n.

(e) Except for α, phenomenological coefficients at the solid surface are extrapolated via

$$\vartheta(n) = (\vartheta_l - \vartheta_g)\frac{n - n_g}{n_l - n_g} + \vartheta_g, \quad (3.2)$$

where ϑ can be the slip coefficient β, surface heat conductivity λ_s', Kapitza resistance κ, or cross-coupling parameter χ. Here, ϑ_l (ϑ_g) is the value of a surface parameter in the homogeneous liquid (gas) phase, i.e., $\vartheta_l \equiv \vartheta(n_l)$ [$\vartheta_g \equiv \vartheta(n_g)$], and n_l (n_g) is the number density of the homogeneous liquid (gas) at liquid-gas coexistence. At temperature $T = 0.875T_c$, the van der Waals theory gives $n_l \approx 0.58/v_0$ ($n_g \approx 0.122/v_0$).

(f) In the limit of $\lambda_w \to \infty$, the solid temperature T_w becomes a constant, and the boundary condition for fluid temperature is given by Eq. (2.43).

B. Flow geometry and initial state

Numerical simulations are carried out in the two-dimensional xz plane with the two fluid-solid interfaces defined at $z = 0$ and L_z as shown in Fig. 1. Details of our numerical algorithm are presented in the Appendix. The state variables n, $\mathbf{v}$, and T in the fluid are defined in a two-dimensional unstaggered uniformly discretized Cartesian mesh. The mesh size of our simulation cell is chosen to be $\Delta x = \Delta z = 0.5\ell$, with $\ell = (C/2k_B v_0)^{1/2}$ being the characteristic liquid-gas interfacial thickness far from the critical point. In the figures below, the x axis is in the horizontal direction, and the z axis is in the vertical direction with $0 \leqslant x \leqslant L_x = 250\ell$ and $0 \leqslant z \leqslant L_z = 60\ell$. The width L_x and height L_z of the computational domain are chosen to be large enough in order to avoid possible boundary effects. The system is closed by applying the periodic boundary condition in the x direction. An estimate for water gives $\ell \cong 1$ nm [79]. Therefore, the droplets simulated in the present paper are of the size of a few tens of nanometers.

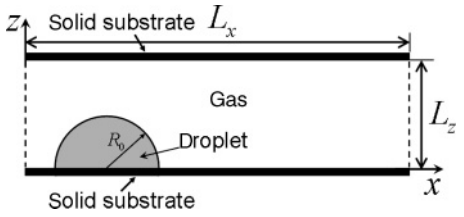

FIG. 1. A schematic for the two-dimensional system in numerical simulations. Bottom: A semicircular liquid droplet of radius R_0 is placed on the flat rigid solid surface at $z = 0$ and is surrounded by gas. Here, the two solid surfaces are parallel to the xy plane. The system is closed by applying the periodic boundary condition in the x direction.

The initial state of the droplet is prepared as follows. A semicircular droplet of radius R_0 is placed on the bottom surface $z = 0$ and is surrounded by gas as shown in Fig. 1. (The droplet is actually infinitely long in the third direction perpendicular to the xz plane.) The fluid temperature is at $T = 0.875T_c$ in the beginning. The temperatures of the top and bottom solid substrates are fixed at $T_w = 0.875T_c$. The liquid and gas densities take the values at liquid-gas coexistence, given by $n_l \approx 0.58/v_0$ and $n_g \approx 0.122/v_0$ at $T = 0.875T_c$. The wettability number $\mathcal{W} \equiv c_s/k_B\ell$ (defined in the Appendix as a dimensionless parameter related to the wettability of solid substrates) is uniform and constant at $z = 0$ in the partial wetting regime. Under these conditions, we wait until the droplet arrives at an almost equilibrium state with a fixed contact angle, hereafter denoted by θ_s, the static contact angle. We want to point out that we have not waited until the whole system reaches the true equilibrium state. Actually, this would take $t \sim 10\,000\tau_0$, which is much larger than the transient time scale $1000\tau_0$ for the droplet migration considered in this paper. (The time unit τ_0 will be defined in Sec IV A.) In fact, true equilibrium states are rarely reached in most practical situations. For different values of $\mathcal{W}$, we record the corresponding static contact angles, which are measured by fitting the level curve of $n = (n_l + n_g)/2$ with a circular arc. We find that $\cos\ \theta_s \cong -6.23\ \mathcal{W}$ (see Fig. 2). It is also observed that, in one-component liquid-gas systems, the contact angle increases with the heat flux (see Fig. 8), a phenomenon that has been theoretically predicted and has been experimentally confirmed [70,80,81].

After this equilibration stage, we set $t = 0$ as the origin of the time axis. A gradient of the wettability number $\mathcal{W}$ is introduced at $t = 0$ to the bottom surface $z = 0$. This is to produce a solid substrate with a constant wettability gradient. Droplet migration induced by this gradient is recorded for the presentation and discussion in the next section.

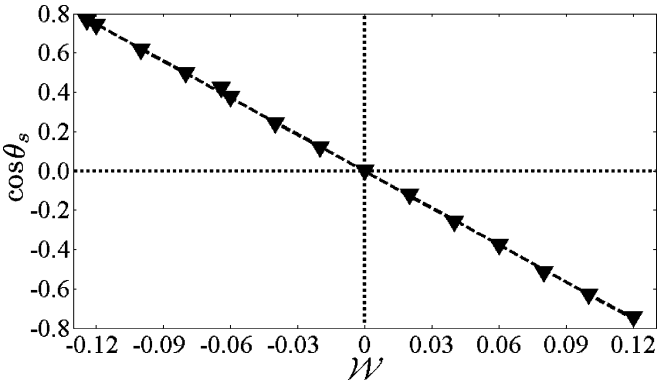

FIG. 2. Cosine of the static contact angle, cos θ_s, is plotted as a function of the wettability number $\mathcal{W}$. The * symbols are measured by fitting the level curve of $n = (n_l + n_g)/2$ with a circular arc. Each symbol corresponds to a nearly equilibrium state of a droplet on a homogeneous solid substrate with the fixed temperature $T_w = 0.875T_c$ and a constant value of $\mathcal{W}$. Dashed line: A linear least squares fitting gives cos $\theta_s = -6.23\mathcal{W}$.

IV. RESULTS AND DISCUSSION

In this section, we present and discuss the numerical results obtained for the migration of droplets on solid substrates with wettability gradients. First, we select a few relevant dimensionless parameters from a large number of those appearing in the nondimensionalized equation system (see the Appendix). For the droplet migration induced by the wettability gradient, the most important parameters are the wettability number $\mathcal{W} = c_s/k_B\ell$ (related to the wettability of a solid substrate), $Ls_l = ls_l/\ell$ (the ratio of the slip length $ls_l = \eta_l/\beta_l$ of the liquid to the length scale ℓ), and the scaled temperature k_BT_w/ε of the bottom substrate. Effects of these parameters are to be presented and discussed below. As for the other dimensionless parameters, we simply set them at physically reasonable values. These include $\mathcal{W} = 0.0$, $Ls_l = 1.0$, and $T_w = 0.875T_c$ at the top substrate, and $\mathcal{R} = 0.06$, $\mathcal{A} = 0.002$, $\Lambda_{sl} = 0.002$, $\mathcal{C}_{qv} = 0.002$, $L_{Kl} = 1.0$, and $\vartheta_{gl} \equiv \vartheta_g/\vartheta_l = 0.5$, where ϑ can be the slip coefficient β, surface heat conductivity λ_s', Kapitza resistance κ, or cross-coupling parameter χ.

Explanations for our choices of parameter values are as follows:

(a) In the limit of $\alpha \to 0$, or equivalently $\mathcal{A} \equiv \alpha k_B\nu/\ell C\varepsilon \to 0$ [40], the wettability condition is described by Eq. (2.26). Then, the dimensionless parameter $\mathcal{W} \equiv c_s/k_B\ell = 0$ leads to $\nabla_\gamma n = 0$ at the fluid-solid interface. This gives a 90° static contact angle. The dependence of the static contact angle θ_s on the dimensionless parameter $\mathcal{W}$ (or the dimensional parameter $c_s = k_B\ell\mathcal{W}$) is shown in Fig. 2.

(b) Typically, the velocity slip length ls_l and the temperature slip length l_{Kl} range between several angstroms and several nanometers in Lennard-Jones fluids [55,82]. Therefore, the dimensionless parameters $Ls_l \equiv ls_l/\ell = 1.0$ and $L_{Kl} \equiv l_{Kl}/\ell = 1.0$ correspond to $ls_l = \ell$ and $l_{Kl} = \ell$ with $\ell \sim 1$ nm. The influence of the slip length will be demonstrated in the physically reasonable range.

(c) The dimensionless parameter $\mathcal{R}$ is defined by $\mathcal{R} \equiv \nu^2 m/\varepsilon\ell^2 = \nu m V_0/\varepsilon\ell$, with ν being the kinematic viscosity independent of the density. This is the only dimensionless parameter in the dimensionless hydrodynamic equations in the bulk region (see the Appendix). For He^3, the critical temperature is $T_c = 3.32$ K from which the energy parameter $\varepsilon = 27k_BT/8$ is determined. Hence, $\mathcal{R}^{1/2}\ell \equiv \sqrt{m/\varepsilon}\nu \approx 2$ Å is obtained. Using $\ell \approx 1$ nm, we then have $\mathcal{R} \approx 0.04$ for He^3 [43]. In the present paper, we used $\mathcal{R} = 0.06$, which was also used in Refs. [67,70].

(d) The dimensionless parameters $\Lambda_{sl} = 0.002$ and $\mathcal{C}_{qv} = 0.002$ are very small. This is to avoid any appreciable effects caused by interfacial heat conductance and mechanical-thermal cross coupling. Whereas, they are permitted by the hydrodynamic boundary conditions, a quantitative study of their physical effects is beyond the scope of the present paper.

A. Migration velocities of the droplets on solid substrates with wettability gradients

According to Brochard [16], as the driving force due to the wettability gradient is balanced by the viscous drag force, the droplet attains a steady state characterized by an almost constant migration velocity $V_{\rm mig}$. In our numerical simulations, such a steady state is obtained after $t \sim 1000\tau_0$ as shown in Fig. 3 where the migration velocity is measured according to $V_{\rm mig} \equiv \frac{1}{h_0}\int_0^{h_0} dz\ v_x$. Here, v_x denotes the $x$component of the fluid velocity measured on the middle line of the droplet, and h_0 is the height of the droplet defined along the middle line (see Fig. 4). The time unit used here is $\tau_0 \equiv \ell^2/\nu$, the viscous relaxation time over the length ℓ. From τ_0, the velocity unit V_0 is then defined by $V_0 \equiv \ell/\tau_0 = \nu/\ell$.

Figure 4 shows the droplet shapes in the beginning ($t = 0$) and in the steady state ($t = 6000\ \tau_0$). In either the hydrophilic case (a) or the hydrophobic case (b), $d\ \cos\ \theta_s/dx \approx 1.5 \times 10^{-3}/\ell$ (with the $+x$ direction as the direction of increasing wettability), $Ls_l = 2.0$, and $T_w = 0.875T_c$ (for the ordinary substrate) are used. It is observed that, compared to the initial shape, a moving droplet experiences a little deformation with elongation in the x direction and contraction in the z direction. And the deformation in the hydrophilic case is more visible than that in the hydrophobic case. The observed deformation is not surprising because the volume of a droplet is almost invariant in migration, and the driving

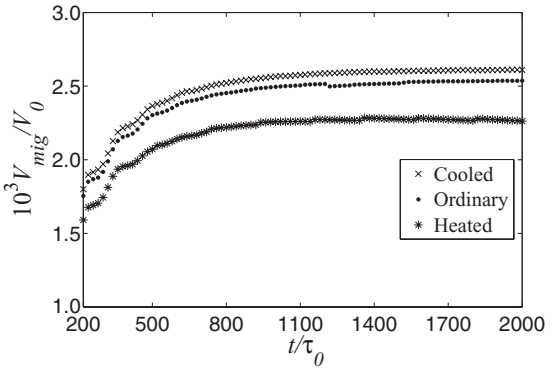

FIG. 3. Time variation in the migration velocity $V_{\rm mig}$. Three different temperatures are used for the bottom substrate with the cooled substrate: dots for $T_w = 0.870T_c$, the ordinary substrate: stars for $T_w = 0.875T_c$, and the heated substrate: crosses for $T_w = 0.890T_c$.

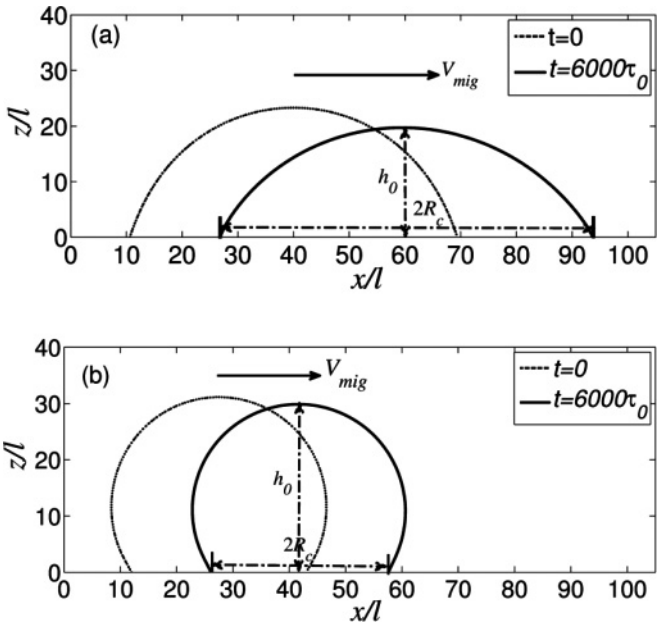

FIG. 4. The $+x$ direction: level curves of $n = (n_l + n_g)/2$ for droplets moving on solid substrates in the direction of increasing wettability. (a) The hydrophilic case with $\theta_s < 90^\circ$. (b) The hydrophobic case with $\theta_s > 90^\circ$. In both cases, $R_0 = 25\ell$, $\frac{d\cos\theta_s}{dx} \approx 1.5 \times 10^{-3}/\ell$, $Ls_l = 2.0$, and the ordinary substrate: $T_w = 0.875T_c$ are used. Here, the droplet height h_0 is defined along the middle line, and R_c is designated as the contact radius.

force arises from the wettability gradient in the x direction at the bottom substrate. In addition, by plotting more droplet shapes between $t = 0$ and $t = 6000\tau_0$ (not shown here), it is found that the deformation of a droplet is actually completed in the initial transient stage ($0 \leqslant t \leqslant 1000\tau_0$).After $t \sim 1000\tau_0$, the droplet *slides* smoothly on the solid substrate. This further specifies the *steady state* observed after $t \sim 1000\tau_0$: It is a state of constant migration velocity and constant shape. A simple comparison between Figs. 4(a) and 4(b) also shows that the droplet moves faster in the hydrophilic case. (This is seen from the two distances covered in the same time period.) This direct observation raises two interesting questions. Why is the droplet moving faster on the hydrophilic substrate? How is the migration velocity affected by the fluid-solid interfacial dynamics? To answer these questions, a more detailed data analysis is needed.

First, the Brochard relation (1.1) has been verified by plotting the migration velocity $V_{\rm mig}$ as a function of $\frac{\gamma h_0}{\eta}\frac{d\cos\theta_s}{dx}$ (see Fig. 5) with $\gamma \approx k_B T(1 - T/T_c)^{3/2}\ell/v_0$ [67]. Note that the interfacial tension of the diffuse liquid-gas interface is temperature dependent. However, we would like to point out that, in one-component fluids, due to the phase transition with latent heat release or absorption, the liquid-gas interface is almost isothermal at the coexistence temperature [43,70]. Consequently, there is no variation in the interfacial tension, and the temperature Marangoni effect is suppressed. On the contrary, the Marangoni effect will play an important role in multicomponent fluids. It is also noted that the assumption of a small contact angle, usually made for theoretical analysis, is not valid here. A linear least squares fitting gives the

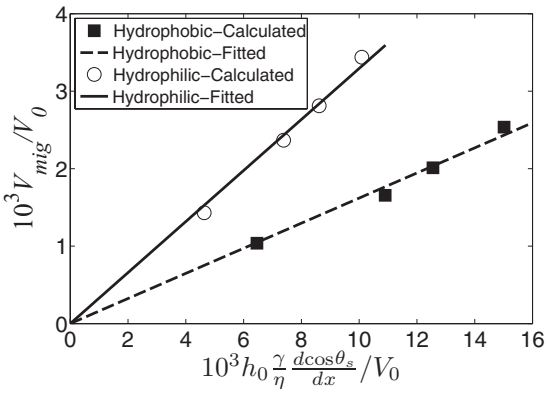

FIG. 5. $V_{\rm mig}$ is plotted as a function of $h_0\frac{\gamma}{\eta}\frac{d}{dx}\cos\theta_s$ for the circles: hydrophilic and for the squares: hydrophobic cases. In both cases, $R_0 = 25\ell$, $Ls_l = 2.0$, and the ordinary substrate $T_w = 0.875T_c$ are used. A linear least squares fitting gives the proportionality coefficient $\alpha_V \approx 0.16$,dashed line: for the hydrophobic case and $\alpha_V \approx 0.33$,solid line: for the hydrophilic case.

proportionality coefficient $\alpha_V \approx 0.16$ for the hydrophobic case and $\alpha_V \approx 0.33$ for the hydrophilic case. This shows again the faster migration of droplets on hydrophilic substrates (under the same other conditions). The agreement of our numerical results with Brochard's scaling analysis implies that the steady droplet migration observed here still results from the balance between the driving force due to the wettability gradient and the viscous drag force.

B. Dependence of the proportionality coefficient α_V on the droplet dynamics

To see why the droplet moves faster on the hydrophilic substrate, we turn to Fig. 6, which shows the tangential velocity v_x, measured on the middle line of the droplet as a function of z. The nonzero derivative $\partial v_x/\partial z$ at the top of the droplet ($z \approx 20\ell$ for the hydrophilic case and $z \approx 30\ell$ for the hydrophobic case) indicates that there is considerable resistance acting on the droplet by the surrounding gas because of the small density ratio and viscosity ratio (both ~ 5) between liquid and gas. Physically, the streamlined shape

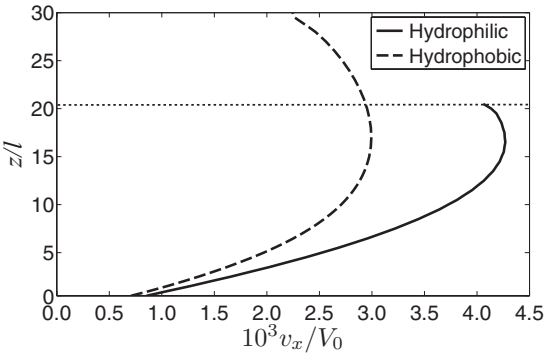

FIG. 6. The tangential velocity v_x, measured on the middle line of the droplet, plotted as a function of z at $t = 2000\tau_0$. The dashed line represents the hydrophobic case ($\theta_s > 90^\circ$) and the solid line represents the hydrophilic case ($\theta_s < 90^\circ$)with $R_0 = 25\ell$, $\frac{d\cos\theta_s}{dx} \approx 1.5 \times 10^{-3}/\ell$, $Ls_l = 2.0$, and the ordinary substrate: $T_w = 0.875T_c$.

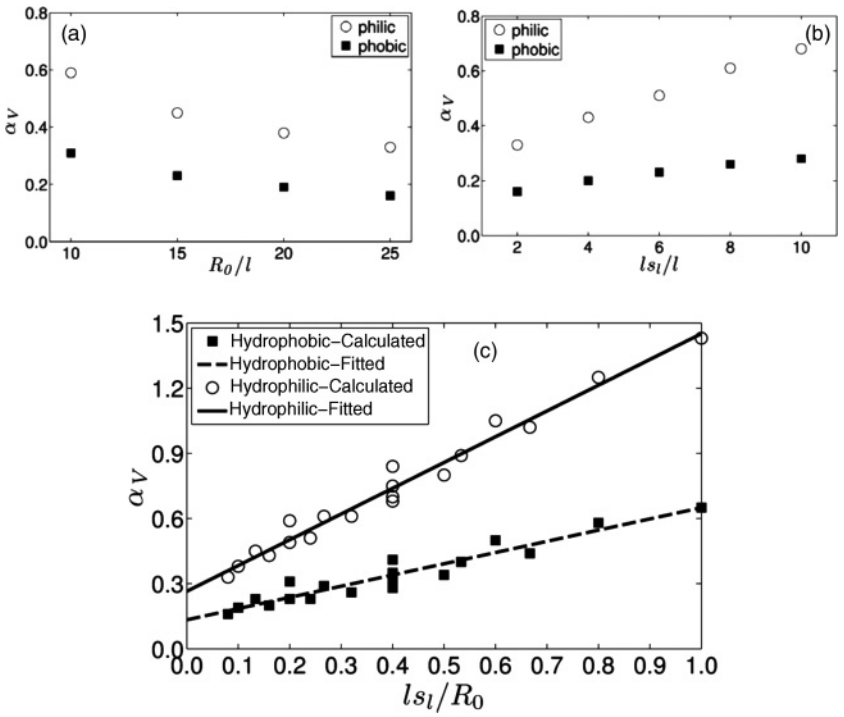

FIG. 7. Dependence of the coefficient α_V on (a) the nondimensionalized initial droplet radius R_0/ℓ for $ls_l/\ell = 2.0$, (b) the nondimensionalized slip length of the liquid $Ls_l = ls_l/\ell$ for $R_0/\ell = 25.0$, and (c) the ratio ls_l/R_0, evaluated for the ordinary substrate: $T_w = 0.875T_c$. A linear least squares fitting gives the solid line for the hydrophilic case and the dashed line for the hydrophobic case in (c). Here, ls_l is the slip length in the liquid phase, given by $ls_l = \nu m n_l/\beta_l$.

of the liquid droplet in the hydrophilic case helps reduce the resistance due to the surrounding gas. This provides a qualitative understanding of why the droplet moves faster in the hydrophilic case (under the same other conditions). Figure 6 also shows that, due to the confinement over a smaller distance in the z direction in the hydrophilic case, the liquid droplet exhibits a larger velocity slip at $z = 0$.

It is worth pointing out that the hydrodynamic boundary conditions are derived in the linear response regime where small displacements from thermodynamic equilibrium are assumed. Accordingly, the microscopic contact angle is close to its equilibrium value in our numerical simulations. It follows that the droplet cannot have a spherical shape in the presence of a wettability gradient. This leads to a gradient of Laplace pressure that drives the motion of the droplet. According to Fig. 6, the tangential velocity v_x plotted as a function of z can be fitted by a quadratic function, which is in agreement with the presence of a pressure gradient. This picture was confirmed in a comparison of asymptotic and numerical results [83].

As already pointed out, the steady droplet migration results from the balance between the driving force due to the wettability gradient and the viscous drag force. Physically, the total viscous drag force is contributed by the viscous dissipation in the bulk region and the dissipation due to velocity slip at the fluid-solid interface. Here, we want to point out that, physically, the interfacial velocity slip provides a mechanism to reduce the *total* dissipation [40,84]. Therefore, it is expected that the droplet migration can be facilitated by the velocity slip. To quantify this effect, we make use of the linear dependence of $V_{\rm mig}$ on $\frac{\gamma h_0}{\eta}\frac{d\cos\theta_s}{dx}$ [5,16,22]. Below, we show the dependence of the coefficient α_V on two length scales: the droplet size (measured by R_0) and the slip length of the tangential velocity slip.

Figure 7(a) shows that α_V decreases with the increasing R_0/ℓ and Fig. 7(b) shows that α_V increases with the increasing $Ls_l = ls_l/\ell$. Physically, it is expected that, in determining the *dimensionless* coefficient α_V, the relative effect of the velocity slip on the reduction of total dissipation is mostly controlled by the *dimensionless* parameter ls_l/R_0. This is indeed shown in Fig. 7(c) where an approximate linear dependence of α_V on small ls_l/R_0 is displayed. The fact that α_V is finite even for zero ls_l/R_0 means there are some other mechanism(s) (e.g., phase transition) operative in resolving the stress singularity associated with the moving contact line [40]. That α_V increases with the increasing ls_l/R_0 confirms that the velocity slip helps to reduce the total dissipation and, hence, to enhance the droplet mobility.

C. Slip versus phase transitions: Droplet migration on cooled, ordinary, and heated solid substrates

Now, we turn to the situation where the substrate temperature is different from the liquid-gas coexistence temperature, and therefore, thermal singularity appears [31–34]. Figure 8 shows the density and velocity fields for a droplet on a solid substrate with and without a wettability gradient. Three different values are used for the bottom substrate temperature T_w: $0.870T_c$ for the cooled substrate, $0.875T_c$ for the ordinary substrate, and $0.890T_c$ for the heated substrate, as shown in Fig. 3. Note that the fluid temperature is at $T = 0.875T_c$ in the beginning, and the temperature of the top substrate is fixed at $0.875T_c$. For the droplet on the cooled substrate with $T_w = 0.870T_c$, condensation, which is characterized by a converging velocity field, occurs in a narrow region near the contact line [see Fig. 8(a1) for the velocity field and the dashed line in Fig. 9(a1) for the corresponding $\nabla \cdot \mathbf{v}$]. For the droplet on the heated substrate with $T_w = 0.890T_c$, evaporation, which is characterized by a diverging velocity field, is prominent in a narrow region near the contact line [see

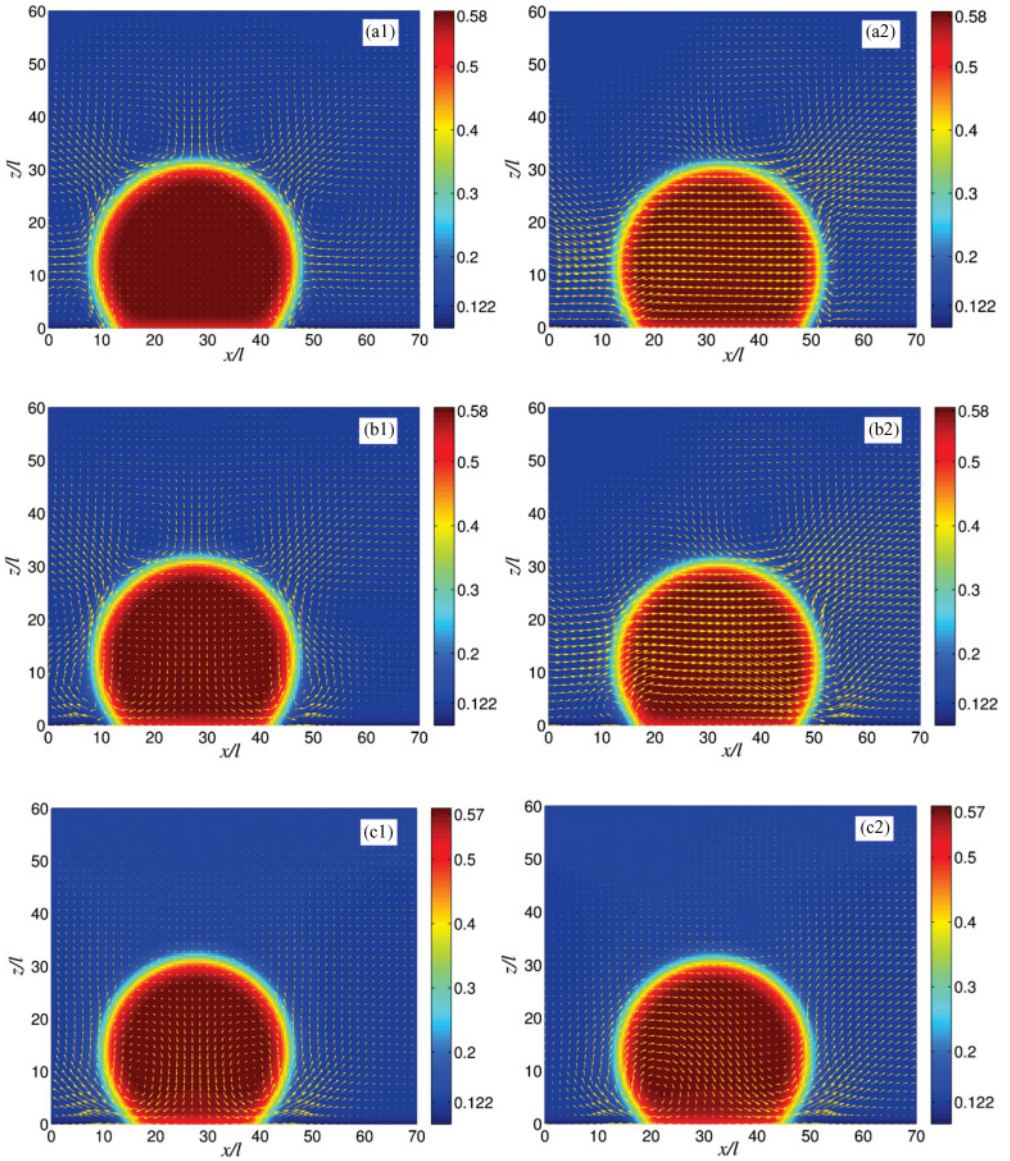

FIG. 8. (Color online) Color: density and arrow: velocity fields for droplets on solid substrates with and without wettability gradients. Each figure is labeled by a letter (a), (b), or (c) for the substrate temperature at $z = 0$ and a number (1) or (2) indicating whether the wettability gradient is 1 for a stationary case: off or 2 for a moving case: on. The substrate temperature at $z = 0$ is set to be the cooled substrate: (a) $0.870T_c$, (b) the ordinary substrate: $0.875T_c$, and (c) the heated substrate: $0.890T_c$. The wettability number $\mathcal{W}$ at the bottom fluid-solid interface $z = 0$ is set to be (1) a homogeneous constant $\mathcal{W} = 0.1$ for the three figures in the left column and (2) a function linear in x, varying from $\mathcal{W} = 0.1$ at $x = 0$ to $\mathcal{W} = 0.04$ at $x = L_x = 250\ell$ for the three figures in the right column. Here, the dimensionless slip length $Ls_l = 2.0$ is used.

Fig. 8(c1) for the velocity field and the dashed line in Fig. 9(c1) for the corresponding $\nabla \cdot \mathbf{v}$]. For the droplet on the ordinary substrate with $T_w = 0.875T_c$, local evaporation is also seen from Fig. 8(b1) and the dashed line in Fig. 9(b1), though less prominent compared to that for the heated substrate. In these observations for droplets on isothermal solid substrates (with T_w being fixed and homogeneous), phase transition (evaporation or condensation) is always concentrated in a narrow region near the contact line, a characteristic in one-component fluids [70]. This is not only observed for the three stationary droplets in the left column of Fig. 8. The moving droplets in the right column of Fig. 8 actually exhibit localized phase transition as well, though less visibly due to the accompanying migration. This will be further discussed with the help of Fig. 9 below. Physically, the localized phase transition is regarded as a manifestation of the thermal singularity concerning temperature distribution [31,46]. It is also interesting to note that the apparent contact angle increases with the increasing substrate temperature as indicated by the decrease in the droplet-substrate contact area in Fig. 8. This is considered to be another characteristic in one-component fluids, which is actually a physical consequence of the first characteristic [70].

To see the effects of wettability gradients, it is noted that, associated with a stationary droplet on a substrate without a wettability gradient, the velocity field appears to be symmetric about the middle line of the droplet. Once

the wettability gradient is turned on, this symmetry must be broken by the droplet migration. This is clearly seen from all three cases in Fig. 8. In addition, the velocity field within a moving droplet appears to be more or less a superposition of (i) a slowly varying velocity field for droplet migration in the direction of increasing wettability (the $+x$ direction) and (ii) the (background) velocity field within the droplet before the wettability gradient is turned on. (This superposition is seen from a comparison between the two figures in each row of Fig. 8.) This is actually mathematically expected based on a leading order expansion in the wettability gradient.

Whereas, the three cases displayed in Fig. 8 all show localized phase transition and (approximate) velocity-field superposition, the velocity fields are quite different for different bottom substrate temperatures. Physically, phase transition and boundary slip are the two competing mechanisms for contact line motion [40]. Therefore, it is expected that the rate of phase transition and the slip velocity profile in the vicinity of the contact line can be greatly affected by the substrate temperature. Below, we present a detailed analysis of the data.

Before we proceed, we point out that, in some hydrodynamic treatments, the liquid-gas transition has been described with the aid of a phenomenological input of the evaporation rate per unit area on the droplet surface J. Some authors used the form $J(r) = J_0/[r_e(t)^2 - r^2]^{1/2}$ for a thin circular droplet as a function of the distance r from the droplet center, where $r_e(t)$ was the droplet radius and J_0 was a constant [59,60]. In recent papers about the spreading with evaporation and condensation in one-component fluids [67,70], this form has been shown to be very different from the simulation results from the dynamic van der Waals theory. For example, evaporation of a thick droplet was found to be mostly localized near the contact line in the partial wetting condition [70]. Our simulations have been carried out in the partial wetting regime as well (see Figs. 2 and 4). It is observed that, on the heated substrate, evaporation is mostly localized near the contact line [see Fig. 8(c)].

Figure 9 shows the profiles of $\nabla \cdot \mathbf{v}$ at $z = 0$ for stationary and moving droplets on the cooled, ordinary, and heated substrates. Since evaporation and condensation are characterized by diverging and converging velocity fields, respectively, $\nabla \cdot \mathbf{v}$

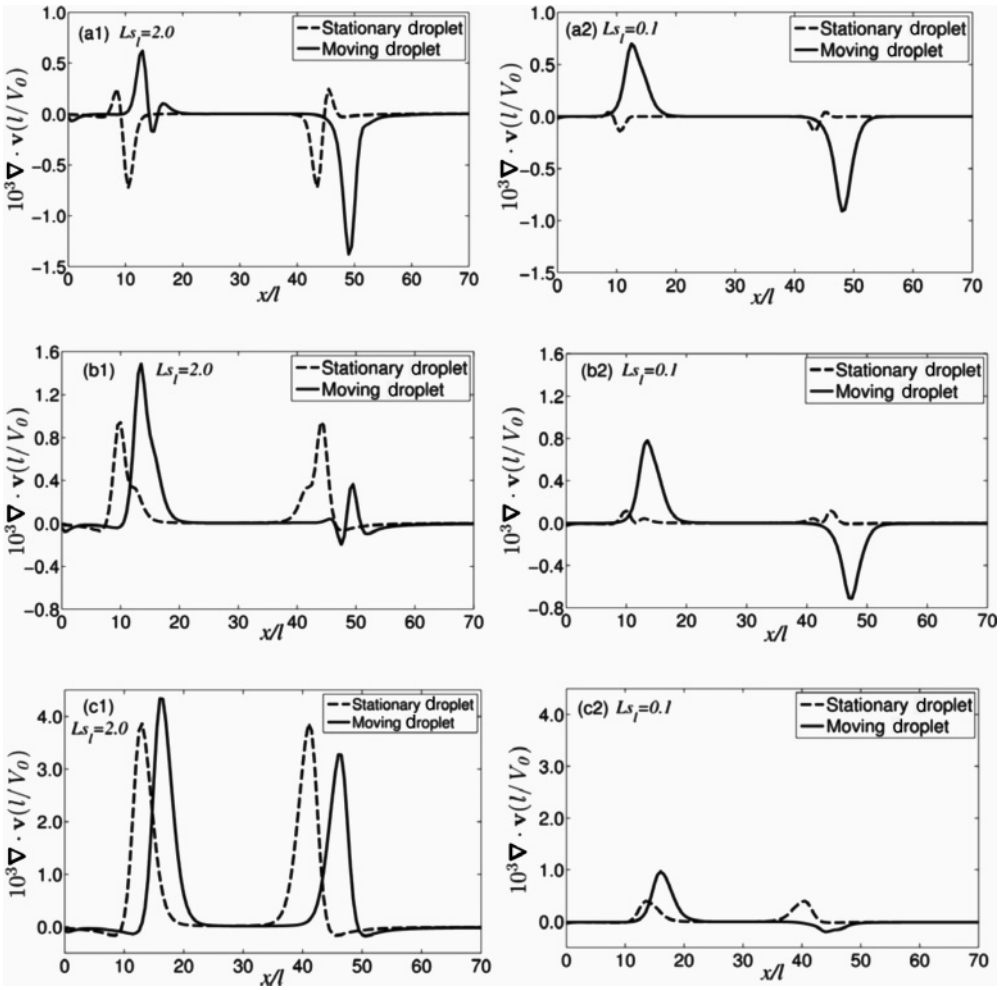

FIG. 9. $\nabla \cdot \mathbf{v}$ at $z = 0$ plotted as a function of x along the solid substrate. Each figure is labeled by a letter (a), (b), or (c) for the substrate temperature at $z = 0$ and a number (1) or (2) indicating whether the slip length is (1) large or (2) small. The substrate temperature at $z = 0$ is set to be (a) the cooled substrate: $0.870T_c$, (b) the ordinary substrate: $0.875T_c$, and (c) the heated substrate: $0.890T_c$. In each figure, the dashed line represents the wettability gradient off: stationary case and the solid line represents the wettability gradient on: moving cases.

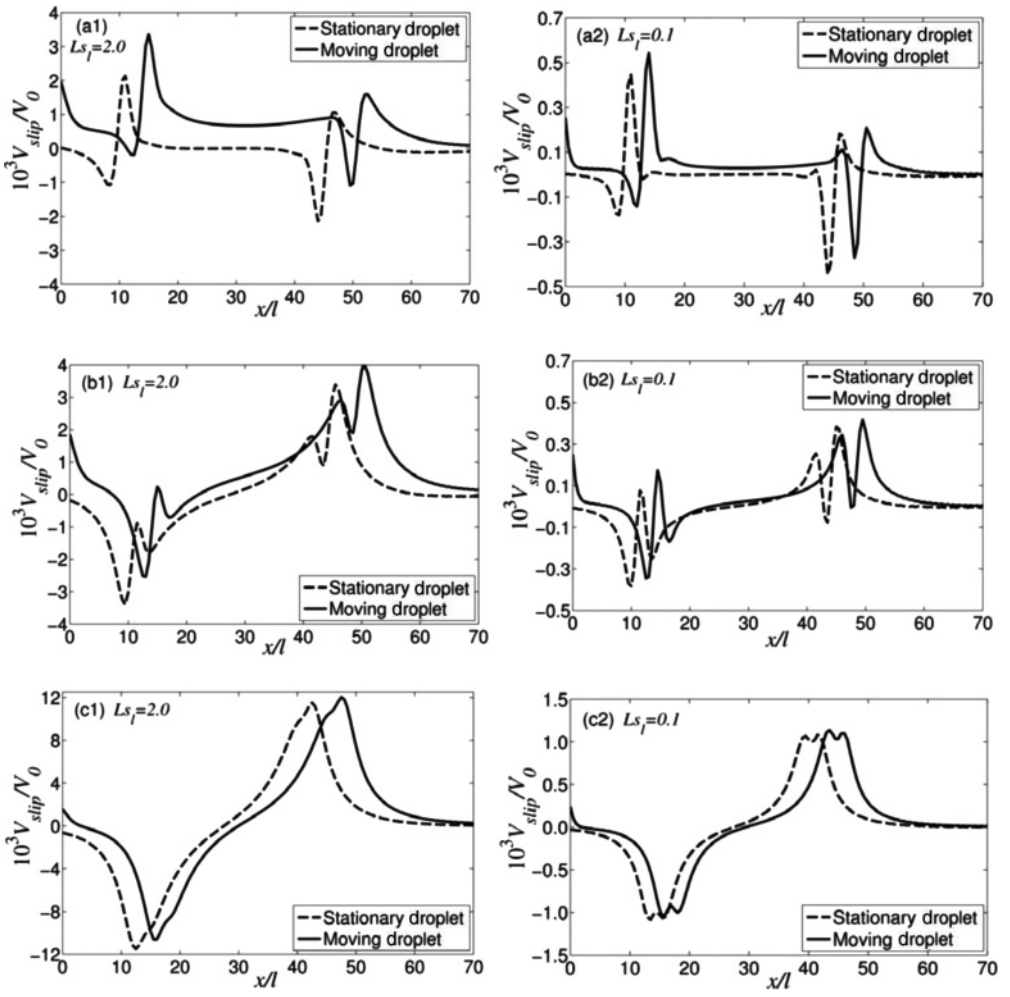

FIG. 10. $V_{\rm slip}/V_0$ plotted as a function of x along the solid substrate. Each figure is labeled by a letter (a), (b), or (c) for the substrate temperature at $z = 0$ and a number (1) or (2) indicating whether the slip length is (1) large or (2) small. The substrate temperature at $z = 0$ is set to be (a) the cooled substrate: $0.870T_c$, (b) the ordinary substrate: $0.875T_c$, and (c) the heated substrate $0.890T_c$. In each figure, the dashed line represents the wettability gradient off: stationary case and the solid line represents the wettability gradient on: moving cases. Figures here have a one-to-one correspondence with those in Fig. 9.

can be taken as a measure of the liquid-gas transition rate. From the dashed lines for stationary droplets and the solid lines for moving droplets, it is evident that liquid-gas transition is always concentrated in a narrow region (of width $\sim 10\ell$) near the contact line.

Although the $\nabla \cdot \mathbf{v}$ profiles are very different for different cases (for stationary and moving droplets on the cooled, ordinary, and heated substrates), the following change is always noted regardless of the substrate temperature. That is, the change in $\nabla \cdot \mathbf{v}$ from a stationary to a moving droplet is always positive around the left contact line but is negative around the right contact line. This means the droplet migration in the $+x$ direction is accompanied by a *net* evaporation around the left contact line and a *net* condensation around the right contact line. Here, the change in $\nabla \cdot \mathbf{v}$ (from a stationary to a moving case) is used to define the net evaporation or condensation relative to the stationary case. According to our previous paper [40], phase transition and boundary velocity slip can both contribute to the contact line motion relative to the solid surface. Here, for the liquid droplet moving in the $+x$ direction, the left contact line moves partly through evaporation, whereas, the right contact line moves partly through condensation. Such transition needed by each moving contact line is just the net evaporation or condensation defined by the change in $\nabla \cdot \mathbf{v}$ as shown in Fig. 9.

Two slip lengths are used in Fig. 9. In the case of small slip length $Ls_l = 0.1$, phase transition is suppressed for stationary droplets, but the change in $\nabla \cdot \mathbf{v}$ from a stationary to a moving case is large. In the case of large slip length $Ls_l = 2.0$, phase transition is noticeable for stationary droplets, but the change in $\nabla \cdot \mathbf{v}$ from a stationary to a moving case is relatively small. This comparison implies that, in moving the contact line, phase transition tends to play a quantitatively more important role if the slip length is reduced. This is consistent with the principle of least energy dissipation (entropy production): As the slip length is reduced, the velocity slip becomes more costly in dissipation, and consequently, the system relies more on phase transition to maintain a moving contact line [40]. This picture can also be demonstrated quantitatively by the slip profiles.

TABLE I. The migration velocity V_{mig} and the stationary-to-moving change in slip velocity ΔV_{slip} (measured at the left contact line) for three substrate temperatures and two slip lengths.

Cases		$10^3 V_{\text{mig}}$	$10^3 \Delta V_{\text{slip}}$
Heated substrate	$Ls_l = 0.1$	1.686	0.028
Ordinary substrate	$Ls_l = 0.1$	1.915	0.095
Cooled substrate	$Ls_l = 0.1$	1.977	0.097
Heated substrate	$Ls_l = 2.0$	2.275	0.920
Ordinary substrate	$Ls_l = 2.0$	2.536	1.115
Cooled substrate	$Ls_l = 2.0$	2.609	1.218

Figure 10 shows the slip velocity profiles for stationary and moving droplets on the cooled, ordinary, and heated substrates. Here, the slip velocity V_{slip} is simply given by v_x at $z = 0$. Although the V_{slip} profiles are very different for different cases (for stationary and moving droplets on the cooled, ordinary, and heated substrates), the following trend is always noted regardless of the substrate temperature: The overall change in the V_{slip} profile from a stationary to a moving case is always upward (i.e., in the $+x$ direction). This means the droplet migration in the $+x$ direction engages boundary slip as a participating mechanism.

Table I shows the migration velocity V_{mig} and the stationary-to-moving change in slip velocity ΔV_{slip} (measured at the left contact line) for three substrate temperatures and two slip lengths. It is seen that V_{mig} and ΔV_{slip} both increase with the increasing slip length. This is consistent with the principle of least energy dissipation (entropy production): As the slip length is increased, the velocity slip becomes less costly in dissipation, and consequently, the droplet acquires a higher mobility by relying more on the boundary slip [40]. This is also consistent with Fig. 9, which shows that the system relies more on phase transition as the slip length is reduced.

To summarize, it has been observed that, for droplets moving on cooled, ordinary, and heated substrates with wettability gradients, the contact lines move through both phase transition and boundary slip with their relative contributions mostly controlled by the slip length. This agreed with the conclusion of our previous paper [40], which was reached for two-phase Couette flows confined between two parallel planar solid walls.

V. CONCLUDING REMARKS

A continuum hydrodynamic model has been presented, suitable for the study of droplet motion in one-component fluids on solid substrates. The model can deal with the thermal singularity, which appears inevitably as the substrate temperature is different from the liquid-gas coexistence temperature. Numerical simulations have been carried out for substrates with homogeneous temperature and wettability gradients. It has been shown that droplets migrate in the direction of increasing wettability as theoretically predicted and experimentally confirmed. The migration velocity is found to satisfy the Brochard relation (1.1) even for droplets on hydrophobic substrates (with large contact angles). The (mobility) coefficient α_V is found to be controlled by the ratio of slip length to droplet radius. These results indicate that the steady migration of a droplet results from the balance between the driving force due to the wettability gradient and the viscous drag force. Furthermore, the velocity field within a moving droplet exhibits a superposition of (i) a slowly varying velocity field for droplet migration in the direction of increasing wettability and (ii) the velocity field within the stationary droplet before the wettability gradient is turned on. Moving contact lines are naturally in droplet migration. From the distributions of velocity divergence and slip velocity, it is observed that phase transition and boundary slip are both engaged in moving the contact lines and the droplets with their relative contributions mostly controlled by the slip length according to the principle of least energy dissipation (entropy production).

We would like to conclude with a few remarks. (i) The droplets in our two-dimensional simulations are actually liquid columns, which are simple but not practical. Brochard [16] and Sekimot *et al.* [85] have shown the instability for liquid cylinders, which can lower the surface energy by breaking into droplets. More realistic results demand large scale three-dimensional simulations. (ii) Isothermal substrates, homogeneous in temperature, are used in the present paper. To be more realistic, heat conduction in the solid needs to be taken into account. This may lead to the issues related to (tangential) temperature gradient, finite substrate thickness, and finite heat conductivity of the solid. (iii) The role of Kapitza resistance (fluid-solid interfacial thermal resistance) and that of the long-range van der Waals force between fluid and solid are worth exploring in the future. Papers in these directions are currently underway.

ACKNOWLEDGMENTS

We would like to thank Professor C. Liu of Penn State University for valuable discussions. This publication is based on work partially supported by Award No. SA-C0040/UK-C0016, presented by King Abdullah University of Science and Technology (KAUST) and Hong Kong RGC Grant No. 603510. X. Xu was partially supported by the Nano Science and Technology Program at HKUST.

APPENDIX: NUMERICAL IMPLEMENTATION

In this appendix, we present our numerical method for solving the continuum model, which consists of the hydrodynamic equations (2.9), (2.10), and (2.15) with the constitutive relations (2.12), (2.13), and (2.14), supplemented by the kinematic boundary condition $v_\gamma = 0$ and the dynamic boundary conditions (2.39), (2.40), and (2.43). (The artificial parasitic flows can be avoided by using Eq. (2.15) for $\hat{S}$ instead of Eq. (2.11) for e_T [70].) Note that Eqs. (2.5) and (2.8) for the generalized pressure are needed by Eq. (2.12), and Eq. (2.16) gives the local temperature as a function of n, ∇n, and $\hat{S}$. Special attention is paid to the application of boundary conditions, and our calculations are carried out for two-dimensional systems (in the xz plane as shown in Fig. 1).

1. Dimensionless equations

To obtain the dimensionless continuum model, we scale the length by $\ell = (C/2k_B v_0)^{1/2}$, which is the characteristic

liquid-gas interfacial thickness far from the critical point, the velocity by $V_0 \equiv \nu/\ell$ (with ν being the kinematic viscosity), the time by $\tau_0 \equiv \ell/V_0$, the number density n by $1/v_0$, the mass density mn by m/v_0, the stresses $-\overleftrightarrow{\Pi}$ and $\overleftrightarrow{\sigma}$ by ε/v_0, the entropy density $\hat{S}$ by k_B/v_0, the temperature by ε/k_B, the interfacial free energy density f_s' by $c_s\varepsilon/k_B v_0$, the tangential wall force F_x by $\nu m V_0/v_0\ell$, and the surface coefficients $\beta(n)$, $\kappa(n)$, $\chi(n)$, and $\lambda_s'(n)$ by their values in the homogeneous liquid phase, i.e., $\beta_l \equiv \beta(n_l)$, $\kappa_l \equiv \kappa(n_l)$, $\chi_l \equiv \chi(n_l)$, and $\lambda_{sl}' \equiv \lambda_s'(n_l)$, respectively. In the dimensionless system, the continuity equation (2.9) reads

$$\frac{\partial n}{\partial t} + \nabla \cdot (n\mathbf{v}) = 0, \tag{A1}$$

the momentum equation (2.10) reads

$$\frac{\partial}{\partial t}(n\mathbf{v}) + \nabla \cdot (n\mathbf{v}\mathbf{v}) = \mathcal{R}^{-1}\nabla \cdot (-\overleftrightarrow{\Pi} + \overleftrightarrow{\sigma}), \tag{A2}$$

and the balance equation (2.15) for entropy density $\hat{S}$ becomes

$$\frac{\partial \hat{S}}{\partial t} + \nabla \cdot (\hat{S}\mathbf{v}) = 2\nabla \cdot (n\nabla n \nabla \cdot \mathbf{v}) + \frac{1}{T}(\overleftrightarrow{\sigma} : \nabla \mathbf{v}) + \left[\nabla \cdot \left(\frac{n}{T}\nabla T\right) + \frac{n}{T^2}(\nabla T)^2\right], \tag{A3}$$

with the dimensionless stresses and pressure given by

$$\overleftrightarrow{\sigma} = \mathcal{R}[n(\nabla \mathbf{v} + \nabla \mathbf{v}^T) + n\overleftrightarrow{\mathbf{I}}\nabla \cdot \mathbf{v}/3], \tag{A4}$$

$$-\overleftrightarrow{\Pi} = -2T\nabla n \nabla n - \hat{p}\overleftrightarrow{\mathbf{I}}, \tag{A5}$$

$$\hat{p} = \frac{nT}{1-n} - n^2 - T|\nabla n|^2 - 2Tn\nabla^2 n. \tag{A6}$$

Equation (2.16) for calculating T from $\hat{S}$ becomes

$$T = \left[\frac{n}{1-n}\exp\left(\frac{\hat{S} + |\nabla n|^2}{n}\right)\right]^{2/3}. \tag{A7}$$

The dimensionless kinematic boundary condition is

$$v_\gamma = 0,$$

with $v_\gamma = -v_z$ at $z = 0$ and $v_\gamma = v_z$ at $z = L_z$, the dimensionless equation (2.39) for the relaxation of n at the fluid-solid interface reads

$$\mathcal{A}\dot{n} = -T\nabla_\gamma n - \frac{\mathcal{W}}{2}T, \tag{A8}$$

with $\nabla_\gamma = -\partial/\partial z$ at $z = 0$ and $\nabla_\gamma = \partial/\partial z$ at $z = L_z$, the dimensionless slip boundary condition (2.40) reads

$$\beta v_x^{\text{slip}} = \mathcal{L}_s\left(-F_x - \mathcal{R}^{-1}\mathcal{C}_{qv}\frac{\beta\chi}{T}\nabla_x T\right), \tag{A9}$$

with $\nabla_x \equiv \partial/\partial x$, $F_x = n\nabla_\gamma v_x - 2\mathcal{R}^{-1}T\nabla_\gamma n \nabla_x n - \mathcal{R}^{-1}\mathcal{W}\nabla_x f_s'$, and $\nabla_x f_s' = (n - n_c)\nabla_x T + T\nabla_x n$, and the dimensionless boundary condition (2.43) for fluid temperature becomes

$$-n\nabla_\gamma T + \mathcal{L}_K^{-1}\kappa^{-1}\left(\frac{1}{T} - \frac{1}{T_w}\right) = -\mathcal{W}T(n - n_c)\nabla_x v_x - \Lambda_{sl}\nabla_x\left(\lambda_s'\nabla_x T\right) - \mathcal{L}_s\left[\mathcal{R}\frac{1}{\beta}F_x^2 + \mathcal{C}_{qv}\nabla_x(\chi F_x) + \mathcal{C}_{qv}\frac{\chi}{T}F_x\nabla_x T\right]. \tag{A10}$$

The dimensionless surface coefficients are given by

$$\vartheta(n) = (1 - \vartheta_{gl})\frac{n - n_g}{n_l - n_g} + \vartheta_{gl}, \tag{A11}$$

where $\vartheta_{gl} \equiv \vartheta_g/\vartheta_l$, ϑ can be the slip coefficient β, surface heat conductivity λ_s', Kapitza resistance κ, or cross-coupling parameter χ.

In the dimensionless equations presented above, there are a number of dimensionless parameters:

(a) $\mathcal{R} = \nu^2 m/\varepsilon\ell^2$.

(b) $\mathcal{A} = \alpha k_B \nu/C\varepsilon\ell$, which is proportional to the damping coefficient α.

(c) The dimensionless substrate temperature T_w.

(d) The wettability number $\mathcal{W} = c_s/k_B\ell$, which measures the wettability of a solid substrate.

(e) $\mathcal{L}_s = \nu m/\beta_l v_0 \ell$, which measures the strength of viscous coupling between fluid and solid. Note that $\mathcal{L}_s$ is related to $Ls_l \equiv ls_l/\ell$ via $Ls_l = n_l v_0 \mathcal{L}_s$, where $ls_l \equiv \eta_l/\beta_l$ (with $\eta_l = \nu m n_l$) is the slip length of the liquid.

(f) $\mathcal{L}_K = \nu\kappa_l\varepsilon^2/\ell v_0 k_B$, which measures the strength of the thermal coupling between fluid and solid. Note that $\mathcal{L}_K$ is related to $L_{Kl} \equiv l_{Kl}/\ell$ via $L_{Kl} = n_l v_0 k_B^2 T_c^2 \mathcal{L}_K/\varepsilon^2$, where $l_{Kl} \equiv \kappa_l\lambda_l T_c^2$ (with $\lambda_l \equiv k_B\nu n_l$) is the Kapitza length [55,56] of the liquid near the critical point.

(g) $\Lambda_{sl} = \lambda_{sl}' v_0/\nu k_B \ell$.

(h) $\mathcal{C}_{qv} = \chi_l\beta_l v_0/\varepsilon\ell$, which measures the strength of mechanical-thermal cross coupling.

(i) The dimensionless surface parameters: $\beta_{gl} = \beta_g/\beta_l$, $\kappa_{gl} = \kappa_g/\kappa_l$, $\lambda_{sgl}' = \lambda_{sg}'/\lambda_{sl}'$, and $\chi_{gl} = \chi_g/\chi_l$.

2. Finite-difference scheme

Below, we present the finite-difference scheme for solving the nondimensionalized system in the xz plane with an emphasis on the use of boundary conditions.

The state variables n, v_x, v_z, and T in the fluid are defined in an unstaggered uniformly discretized Cartesian mesh. The number density n, velocity component v_x, and entropy density $\hat{S}$ are updated at the interior sites and at the fluid-solid interface, whereas, the velocity component v_z is only updated at the interior sites due to the impermeability condition $v_\gamma = 0$ at the fluid-solid interface. This involves the use of hydrodynamic equations (A1)–(A3). Obviously, values of n, v_x, v_z, and T at some "ghost" sites are needed for updating n, v_x, and $\hat{S}$ at the fluid-solid interface and updating v_z at the sites closest to the fluid-solid interface. [Note that, in updating v_z at the sites next to the fluid-solid interface, the term $Tn\nabla^2 n$ in Eq. (A6) for $\hat{p}$ leads to a third-order derivative of n in the z direction, and hence, the values of n at the ghost sites out of the fluid space are needed.] With $\dot{n}$ evaluated in the continuity equation (A1), the ghost values of n can be first determined by the boundary condition (A8) through $\nabla_\gamma n$. The ghost values of v_x are then determined by the boundary condition (A9) through $\nabla_\gamma v_x$. The ghost values of T can be determined by Eq. (A10) through $\nabla_\gamma T$. As for the ghost values of v_z, they are determined through $\nabla_\gamma v_\gamma$ at the fluid-solid interface, which can be evaluated using second-order one-sided extrapolation. Finally, the fluid temperature T can be directly obtained from Eq. (A7).

[1] L. E. Scriven and C. V. Sternling, Nature (London) **187**, 186 (1960).
[2] D. A. Edwards, H. Brenner, and D. T. Wasan, *Interfacial Transport Processes and Rheology* (Butterworth-Heinemann, Boston, 1991).
[3] J. Thomson, Philos. Mag. **10**, 330 (1855).
[4] C. G. M. Marangoni, Ann. Phys. Chem. **143**, 337 (1871).
[5] H. P. Greenspan, J. Fluid Mech. **84**, 125 (1978).
[6] S. B. Carter, Nature (London) **213**, 256 (1967).
[7] M. Grunze, Science **283**, 41 (1999).
[8] B. S. Gallardo, V. K. Gupta, F. D. Eagerton, L. I. Jong, V. S. Craig, R. R. Shah, and N. L. Abbott, Science **283**, 57 (1999).
[9] H. A. Stone, A. D. Stroock, and A. Ajdari, Annu. Rev. Fluid Mech. **36**, 381 (2004).
[10] G. M. Whitesides, Nature (London) **442**, 368 (2006).
[11] A. M. Cazabat, F. Heslot, S. M. Troian, and P. Carles, Nature (London) **346**, 824 (1990).
[12] J. B. Brzoska, F. Brochard-Wyart, and F. Rondelez, Langmuir **9**, 2220 (1993).
[13] M. K. Chaudhury and G. M. Whitesides, Science **256**, 1539 (1992).
[14] N.-T. Nguyen, K. M. Ng, and X. Huang, Appl. Phys. Lett. **89**, 052509 (2006).
[15] K. Ichimura, S. K. Oh, and M. Nakagawa, Science **288**, 1624 (2000).
[16] F. Brochard, Langmuir **5**, 432 (1989).
[17] E. Raphael, C. R. Acad. Sci., Ser. II: Mec., Phys., Chim., Sci. Terre Univers **306**, 751 (1988).
[18] T. Ondarçuhu and M. Veyssie, J. Phys. II **1**, 75 (1991).
[19] F. Domingues Dos Santos and T. Ondarçuhu, Phys. Rev. Lett. **75**, 2972 (1995).
[20] S. Daniel, M. K. Chaudhury, and J. C. Chen, Science **291**, 633 (2001).
[21] S. Daniel and M. K. Chaudhury, Langmuir **18**, 3404 (2002).
[22] S. Daniel, S. Sircar, J. Gliem, and M. K. Chaudhury, Langmuir **20**, 4085 (2004).
[23] R. S. Subramanian, N. Moumen, and J. B. McLaughlin, Langmuir **21**, 11844 (2005).
[24] N. Moumen, R. S. Subramanian, and J. B. McLaughlin, Langmuir **22**, 2682 (2006).
[25] R. D. Deegan, O. Bakajin, T. F. Dupont, G. Huber, S. R. Nagel, and T. A. Witten, Phys. Rev. E **62**, 756 (2000).
[26] K. Ozawa, E. Nishitani, and M. Doi, Jpn. J. Appl. Phys. **44**, 4229 (2005).
[27] C. T. Pham, G. Berteloot, F. Lequeux, and L. Limat, Europhys. Lett. **92**, 54005 (2010).
[28] P. Müller-Buschbaum *et al.*, J. Phys.: Condens. Matter **23**, 184111 (2011).
[29] C. Huh and L. E. Scriven, J. Colloid Interface Sci. **35**, 85 (1971).
[30] E. B. Dussan V. and S. H. Davis, J. Fluid Mech. **65**, 71 (1974).
[31] S. J. S. Morris, J. Fluid Mech. **411**, 59 (2000).
[32] V. S. Ajaev, J. Fluid Mech. **528**, 279 (2005).
[33] V. Ajaev, J. Klentzman, C. Sodtke, and P. Stephan, Microgravity Sci. Technol. **19**, 23 (2007).
[34] P. Colinet and A. Rednikov, Eur. Phys. J. Spec. Top. **197**, 89 (2011).
[35] J. Koplik, J. R. Banavar, and J. F. Willemsen, Phys. Rev. Lett. **60**, 1282 (1988).
[36] P. A. Thompson and M. O. Robbins, Phys. Rev. Lett. **63**, 766 (1989).
[37] M. L. Ford and A. Nadim, Phys. Fluids **6**, 3183 (1994).
[38] T. Qian, X.-P. Wang, and P. Sheng, Phys. Rev. E **68**, 016306 (2003).
[39] T. Qian, X.-P. Wang, and P. Sheng, Phys. Rev. Lett. **93**, 094501 (2004).
[40] X. Xu and T. Qian, J. Chem. Phys. **133**, 204704 (2010).
[41] H.-Y. Chen, D. Jasnow, and J. Viñals, Phys. Rev. Lett. **85**, 1686 (2000).
[42] D. Jacqmin, J. Fluid Mech. **402**, 57 (2000).
[43] A. Onuki, Phys. Rev. E **75**, 036304 (2007).
[44] D. Bonn, J. Eggers, J. Indekeu, J. Meunier, and E. Rolley, Rev. Mod. Phys. **81**, 739 (2009).
[45] A. Onuki, Phys. Rev. Lett. **94**, 054501 (2005).
[46] V. S. Nikolayev, Phys. Fluids **22**, 082105 (2010).
[47] X. Xu, C. Liu, and T. Qian, Commun. Math. Sci. (to be published).
[48] P. C. Hohenberg and B. I. Halperin, Rev. Mod. Phys. **49**, 435 (1977).
[49] D. M. Anderson, G. B. McFadden, and A. A. Wheeler, Ann. Rev. Fluid Mech. **30**, 139 (1998).
[50] D. Jasnow and J. Viñals, Phys. Fluids **8**, 660 (1996).
[51] J. Lowengrub and L. Truskinovsky, Proc. R. Soc. London, Ser. A **454**, 2617 (1998).
[52] N. Vladimirova, A. Malagoli, and R. Mauri, Phys. Rev. E **60**, 6968 (1999).
[53] U. Thiele, S. Madruga, and L. Frastia, Phys. Fluids **19**, 122106 (2007).
[54] T. Laurila, A. Carlson, M. Do-Quang, T. Ala-Nissila, and G. Amberg, Phys. Rev. E **85**, 026320 (2012).
[55] J.-L. Barrat and F. Chiaruttini, Mol. Phys. **101**, 1605 (2003).
[56] Z. Ge, D. G. Cahill, and P. V. Braun, Phys. Rev. Lett. **96**, 186101 (2006).
[57] C. Liu and Z. Li, Phys. Rev. Lett. **105**, 174501 (2010).
[58] D. M. Anderson and S. H. Davis, Phys. Fluids **7**, 248 (1995).
[59] R. D. Deegan, O. Bakajin, T. F. Dupont, G. Huber, S. R. Nagel, and T. A. Witten, Nature (London) **389**, 827 (1997).
[60] H. Hu and R. G. Larson, Langmuir **21**, 3972 (2005).
[61] N. Shahidzadeh-Bonn, S. Rafai, A. Azouni, and D. Bonn, J. Fluid Mech. **549**, 307 (2006).
[62] T. Okuzono, M. Kobayashi, and M. Doi, Phys. Rev. E **80**, 021603 (2009).
[63] D. Bedeaux, Adv. Chem. Phys. **64**, 47 (1986).
[64] A. Oron, S. H. Davis, and S. G. Bankoff, Rev. Mod. Phys. **69**, 931 (1997).
[65] R. Chella and J. Vinals, Phys. Rev. E **53**, 3832 (1996).
[66] P. Yue, C. Zhow, and J. J. Feng, J. Fluid Mech. **645**, 279 (2010).
[67] R. Teshigawara and A. Onuki, Phys. Rev. E **82**, 021603 (2010).
[68] A. Onuki, *Phase Transition Dynamics* (Cambridge University Press, Cambridge, UK, 2002).
[69] J. W. Cahn and J. E. Hilliard, J. Chem. Phys. **28**, 258 (1958).
[70] R. Teshigawara and A. Onuki, Europhys. Lett. **84**, 36003 (2008).
[71] J. S. Rowlinson and B. Widom, *Molecular Theory of Capillarity* (Clarendon, Oxford, 1989).
[72] L. Onsager, Phys. Rev. **37**, 405 (1931).
[73] S. R. De Groot and P. Mazur, *Non-Equilibrium Thermodynamics* (Dover, New York, 1984).
[74] E. M. Lifshitz and L. P. Pitaevskii, *Physical Kinetics* (Butterworth-Heinemann, Oxford, 1981).

[75] M. Han, J. Colloid Interface Sci. **284**, 339 (2005).
[76] P. D. M. Spelt, J. Fluid Mech. **561**, 439 (2006).
[77] H. Ding and P. D. M. Spelt, Phys. Rev. E **75**, 046708 (2007).
[78] J. W. Cahn, J. Chem. Phys. **66**, 3667 (1977).
[79] R. Teshigawara and A. Onuki, Phys. Rev. E **84**, 041602 (2011).
[80] S. J. S. Morris, J. Fluid Mech. **494**, 297 (2003).
[81] J. Hegseth, A. Oprisan, Y. Garrabos, V. S. Nikolayev, C. Lecoutre-Chabot, and D. Beysens, Phys. Rev. E **72**, 031602 (2005).
[82] J.-L. Barrat and L. Bocquet, Phys. Rev. Lett. **82**, 4671 (1999).
[83] L. M. Pismen and U. Thiele, Phys. Fluids **18**, 042104 (2006).
[84] T. Qian, X.-P. Wang, and P. Sheng, J. Fluid Mech. **564**, 333 (2006).
[85] K. Sekimot, R. Oguma, and K. Kawasaki, Ann. Phys. **176**, 359 (1987).